sustainability

Article

Morphometric, Meteorological, and Hydrologic Characteristics Integration for Rainwater Harvesting Potential Assessment in Southeast Beni Suef (Egypt)

Hakeem Musaed [1,2,*], Ahmed El-Kenawy [3] and Mohamed El Alfy [1]

[1] Geology Department, Faculty of Science, Mansoura University, Mansoura 35516, Egypt
[2] Department of Engineering Geology, Faculty of Oil and Minerals, University of Shabwah, Shabwah, Yemen
[3] Department of Geography, Mansoura University, Mansoura 35516, Egypt
* Correspondence: hakeem21112@gmail.com; Tel.: +0020-1119101981

Abstract: In arid areas, the forecast of runoff is problematic for ungauged basins. The peak discharge of flashfloods and rainwater harvesting (RWH) was assessed by the integration of GIS, the RS tool and hydrologic modeling. This approach is still under further improvement to fully understand flashflood and rainwater harvesting potentialities. Different morphometric parameters are extracted and evaluated; they show the most hazardous sub-basins. Vulnerability potential to flooding is high relative to steep slopes, high drainage density, and low stream sinuosity. Using hydrologic modeling, lag time, concentration time, peak discharge rates, runoff volume, rainfall, and total losses are calculated for different return periods. The hydrologic model shows high rainfall rates, and steep slopes are present in the southeastern part of the study area. Low rainfall rates, moderate–high runoff, and gentle slopes are found in the central and downstream parts, which are suitable sites for rainwater harvesting. An analytic hierarchy process is utilized for mapping the best sites to RWH. These criteria use land-cover, average annual max 24 h rainfall, slope, stream order, and lineaments density. About 4% of the basin area has very high potentialities for RWH, while 59% of the basin area has high suitability for RWH. Ten low dam sites are proposed to impact flooding vulnerability and increase rainwater-harvesting potentialities.

Keywords: climate change; rainwater harvesting; arid areas; metrologic analysis; hydrologic modeling; AHP

check for updates

Citation: Musaed, H.; El-Kenawy, A.; El Alfy, M. Morphometric, Meteorological, and Hydrologic Characteristics Integration for Rainwater Harvesting Potential Assessment in Southeast Beni Suef (Egypt). *Sustainability* **2022**, *14*, 14183. https://doi.org/10.3390/su142114183

Academic Editor: Michalis Diakakis

Received: 28 September 2022
Accepted: 27 October 2022
Published: 31 October 2022

1. Introduction

Flashflood evaluation is an important issue for creating suitable development plans in arid regions. Arid or semiarid areas may experience more floods than moist regions with higher rainfall intensity [1]. They are one of the major natural hazards that cause loss of life and economy [2]. In comparison to other natural hazards, flashfloods are the most overwhelming and the highest of the natural tragedies that damage houses, irrigation systems, streets, crops, and tapwater networks, besides causing economic damage in many regions throughout the world. It is reported that nearly 44% of deaths caused by natural hazards worldwide, especially in arid regions, are related to flooding events [3–6].

Although this natural hazard is mainly driven by unexceptional atmospheric conditions, it is largely impacted by other non-climatic variables like topography, urban and vegetation cover, and high-velocity water movements [7–9].

In arid regions, flashfloods are driven by a high variability of rainfall over space and time. Rainfall in arid and semi-arid regions is sporadic and less frequent but more intense when it occurs. Flashfloods commonly occur in valleys that are distinguished by their dry state [10]. In arid regions, monitoring flashfloods is a challenge due to inadequate observational data, absence of monitoring systems, and lack of infrastructure, especially in remote sites. Flashfloods represent a significant source of water in arid regions, and a small part is infiltrated for groundwater [10,11].

The idea of rainwater harvesting (RWH) was used in various portions of the world 3000 years ago. Nevertheless, the utilization of RWH systems declined with the development of technology in the twentieth century. The increasing usage of RWH methods through the last two decades can be attributed to an increasing gap between rising water demands attributable to population growth and declining water supplies due to prospective climatic changes [12–14]. This has resulted in increases in the focus of researchers on the scientific parts and environmental influences of RWH methods [15]. Several methods for RWH and artificial recharge have been proposed, involving the creation of surface basins, the creation of deep channels, and the drilling of recharge wells [16–18].

In arid regions, climate change and the rising water demands for drinking and agricultural and industrial purposes can increase the pressure on limited water resources and clearly represent the water scarcity problems [19,20]. The overexploitation of groundwater in arid areas can cause a decline in water levels [21,22]. Because of the spatial and temporal variability of rainfall in arid areas, normal groundwater recharge is not stable, which constitutes a challenge to proper aquifer sustainability. RWH suggests a good method for improving groundwater resources in these arid areas, which can assist in the depletion of groundwater [14]. Several studies have been carried out related to RWH. Mahmoud et al. (2014) [23] used the analytical hierarchy process (AHP) with five thematic layers to identify RWH-suitable areas in Egypt. Alataway and El Alfy (2019) [14] assessed rainwater harvesting in central Saudi Arabia and determined artificial groundwater recharge potentialities in four dam reservoirs; they correlated the surface water level in these reservoirs and water table measurements in five recharge wells. The AHP technique was also used by Balkhair and Ur Rahman (2021) [24] to create a suitable map for RWH sites in the basin of wadi Al-Lith, Saudi Arabia, where eight appropriate criteria were applied. Ouali et al. (2022) [25] assessed the RWH in the Toudgha basin of southeastern Morocco by using the APH method, wherein the RWH map provides good information to decision-makers on water supply planning.

In the Eastern Desert, Egypt, groundwater is the main source for agriculture and drinking. Drought, climatic change, overpumping and low annual rainfall rates are foremost challenges to farmers. To increase the availability of water resources, harvesting techniques can be used through the construction of low–high dams. Numerous studies were carried out using geographic information system (GIS) and remote sensing (RS) for the assessment of flashfloods [26–29]. Therefore, an assessment of the flashfloods and their drivers are extremely important. The aim of this study is to build a framework for evaluating flashflood risk and rainwater-harvesting potentialities in the east Bani Suef area, Egypt. The main innovative aspects of the current study are to assess rainwater-harvesting potentialities. Specifically, this study proposes an integrated approach, based on a geographic information system (GIS), remote sensing techniques, and morphometric and rainfall–runoff modeling. This study correlates the risk of flashfloods using a morphometric ranking method, as well as the AHP method for the determination of suitable areas of rainwater harvesting in low-terrain arid areas.

2. Study Area

The study area is located in the southeastern part of the Beni Suef Governorate between latitudes 27°10′ N and 28°40′ N and longitudes 30°85′ E and 32°35′ E (Figure 1). It has an area of approximately 10,646 km^2, length of 178 km, and average width of 60 km. The elevation varies between 26 m (asl) at the low-lying zone near the Nile River (western part) and 1266 m in the northeastern part close to the Red Sea Mountains (Figure 1).

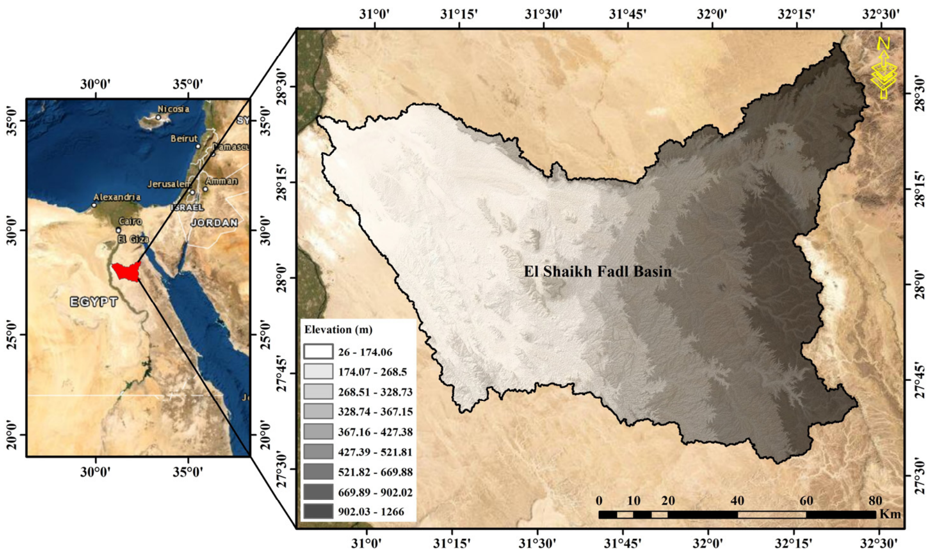

Figure 1. Location map of the study area.

The studied area is situated in the arid zone in the Eastern Desert, with hot summers reaching 40 °C, and cold winters with a minimum temperature near zero °C. Evaporation rates range between 4.8 mm/day in winter to 12.4 mm/day in summer [30,31]. The average annual rainfall ranges between 2.75 mm and >50 mm at the extreme southeastern part. In the last 50 years, floods were recorded in 1969, 1980, 1984, 1985, 1994 and 2020. Nevertheless, the volume of precipitation is quite low, and floods are the foremost natural risk in the Eastern Desert [32,33].

3. Materials and Methods

The used methodology uses three consequent steps. The first one described the morphometric parameters to evaluate the flashflood risk assessment. The second one provided processes of rainfall–runoff modeling. A spatio-temporal lumped model is used to evaluate the runoff volumes for each sub-basin. The third step determined the good locations for rainwater harvesting (Figure 2). These steps were executed through processing spatial data, counting digital elevation model DEM, RS, soil, and rainfall–runoff data. Several software packages were used: ArcGIS 10.2 [34], ERDAS Imagine 2015 [35], HyfranPlus [36], WMS 11.1 [37], HEC-HMS 4.5 [38], PCI-Geomatics 2015 [39], ENVI 4.5 [40] and RockWorks 16 [41].

3.1. Rainfall Processing

Daily rainfall data were provided by the Directorate General of Meteorology (DGM) in Egypt for the period 1979–2014. Data were provided for the Beni-Suef meteorological station (29.04° N, 31.09° E). Given the lack of metadata for these observed data, it was crucial to guarantee the accuracy and reliability of the data. The goal was to make weather and climate variability the primary drivers of climate variability, rather than other non-climatic variables (e.g., relocations of observatories, changes in instruments, observers and observation practices, urbanization, etc.) [42]. Therefore, the data went through a rigid quality assurance process. The process was designed to get rid of anomalies and outlier values in the data. In order to test the homogeneity of the data, we applied relative homogeneity tests (which consider data from neighboring stations) in order to identify potential break points in the series. This procedure is recommended when there is a lack of a convincing history and metadata for the meteorological records. In particular, we used a semi-automated protocol by way of the R package HOMER, which is designed for detecting and fixing inhomogeneities in monthly climatic data by means of relative homogeneity techniques [43].

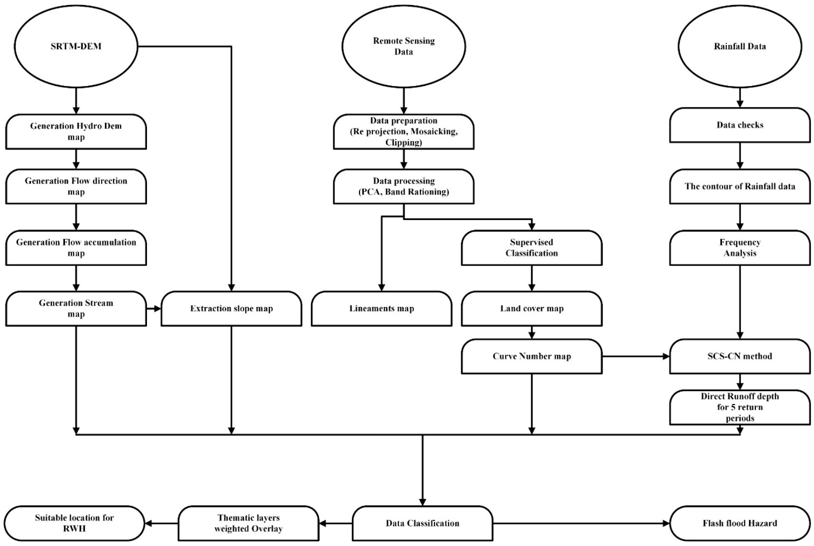

Figure 2. Flow chart of the methodology used for assessing the flashflood hazard and RWH sites.

In light of recent developments in numerical weather prediction modeling and data assimilation, a growing number of reanalysis datasets are available, providing information on a wide range of climate variables with enhanced spatial continuity and long and continuous temporal coverage. Given the scarcity of local meteorological records in the study domain, a decision was made to employ the National Center for Environmental Prediction's (NCEP) Climate Forecast System Reanalysis (CFSR) [44]. Based on a fully coupled ocean–land–atmosphere model, the NCEP-CFSR reanalysis dataset (https://www.ncdc.noaa.gov/data-access/model-data/model-datasets (accessed on 14 February 2022)) is used to assimilate and predict atmospheric states through the application of numerical weather prediction techniques [44]. NCEP-CFSR (hereinafter CFSR) has been widely used in hydroclimatic analysis and simulation, especially in regions with sparsely distributed weather stations, due to its improved spatial resolution (0.5°) and relatively long time series (1979 onwards) [45] Herein, it is noteworthy that several reanalysis datasets are available for research community, such as the National Centers for Environmental Prediction reanalysis II (NCEP-2), the European Centre for Medium-Range Weather Forecasts (ECMWF) Interim Reanalysis (ERA-Interim), the Japanese 55-year Reanalysis Project (JRA-55), and the National Aeronautics and Space Administration (NASA) Modern Era Reanalysis for Research and Applications Version-2 (MERRA-2). However, in our study, the preference was made to employ the CFSR dataset for characterizing flashfloods because of its uniform spatial and temporal resolutions across a wide range of hydrometeorological variables that contribute significantly to rainfall-harvesting assessment, including maximum and minimum air temperatures, precipitation, etc. In this work, the spatiotemporal distribution of precipitation in each sub-basin within the study domain was analyzed by selecting the adjacent gridded data. The events were assigned one of five fictitious proposal storms with return periods of 5, 10, 25, 50, and 100 years. Then, we used statistical frequency analysis to determine the maximum 24 h precipitation values for 5-, 10-, 25-, 50-, and 100-year return periods. Curves for five return periods were fitted using the Log-Pearson type 3, method of moments (BOB), which provides the best-fit curve for the used rainfall data with the smallest root-mean-square error (RMSE). Precipitation spatial analysis for the five previous return periods was performed using the Kriging method.

In order to look at the possible impacts of climate change on rainfall-harvesting capabilities, we assessed long-term changes (1979–2014) in a range of selected climatic variables (e.g., maximum and minimum air temperatures, rainfall totals, relative humidity, etc) (Appendix A, Tables A1–A3). Trends were assessed using the linear least squares regression technique. For each variable and time series under study, we calculated the slope to indicate the rate of change over the period of interest. To determine whether or not the observed changes were statistically significant at the 95% confidence interval ($p < 0.05$), the modified Mann–Kendall statistic was used [44]. This is an example of a non-parametric test, which does not presume anything about the data's distribution in advance. This metric's positive values indicate an increasing trend, while its negative values point to a declining trend. The impact of serial autocorrelation presented in the data on trend detection is limited when using the modified Mann–Kendall test, as opposed to the standard Mann–Kendall test. This is simply due to the fact that the sample size is taken into account, and a correction factor is applied to the original variance formulation when serial autocorrelation is present in the data [43,44].

3.2. Morphometric Analysis [45,46]

The ASTER Digital Elevation Model with 30 m resolution was obtained from the United States Geological Survey (USGS, ASTER). The study area was covered by four USGS DEM quadrangles. Analyses of the ASTER DEM was used to determine watershed delineations, flow directions, flow accumulations, stream orders, morphometric parameters, and ground surface slope.

The morphometric parameters were extracted for the main basin and its sub-basins. These parameters were classified into three types: linear [47–50], areal [47,49,51], and relief [47,49,51–53] (Appendix A, Tables A4–A6). Some morphometric parameters were utilized to evaluate the flashflood hazard using the morphometric ranking method. The morphometric ranking method was used to calculate the degree of the vulnerability to flashflood for each sub-basin [10,54,55]. Fourteen morphometric parameters sensitive to the flooding process were selected. All of these parameters were positively correlated to the hazard degree of flood, while the length of overland flow (Lg), weighed mean bifurcation ratios (WMRb), and mean bifurcation ratio (MRb) were inversely correlated. The morphometric ranking score for each parameter was determined by the following equations:

$$\mathrm{Y} = \frac{(\mathrm{Ymax} - \mathrm{Ymin})(\mathrm{X} - \mathrm{Xmin})}{(\mathrm{Xmax} - \mathrm{Xmin})} + \mathrm{Ymin} \tag{1}$$

For Lg, MRb, and WMRb showing an inverse correlation [56], the degree of hazard was determined by utilizing the following equation;

$$\mathrm{Y} = \frac{(\mathrm{Ymax} - \mathrm{Ymin})(\mathrm{X} - \mathrm{Xmax})}{(\mathrm{Xmin} - \mathrm{Xmax})} + \mathrm{Ymin} \tag{2}$$

where Y is the relative degree of hazard, and Ymax and Ymin are the highest and the lowest limits of the projected scale. Xmax and Xmin are the maximum and minimum assessed values of any parameter. X is the value of any parameter located between the maximum and minimum values [56]. The score for flashflood hazard for each basin ranged from 1 to 5, which was dependent on the parameter relative to the susceptibility of flooding.

3.3. Image Analysis

Multi-spectral satellite images from September 2021 of the Landsat-8 was used (USGS, https://earthexplorer.usgs.gov/ (accessed on 1 September 2021)). It was obtained from USGS with a spatial resolution of 30 m (multi-spectral) and 15 m (panchromatic) and land cloud cover of 0.06%. The mosaicking and clipping bands were made using spatial analyst tools in ArcMap10.2. Resampling the multi-spectral bands with panchromatic band was carried out to increase the spatial and spectral range resolution. Composites bands, band rations, and principle component analyses were completed to determine the soil types, curve number (CN), and land-use classes. Supervised classification was done after the initial unsupervised classification [57,58].

The final output of the image analysis categorized the study area into different classes with different curve numbers. This curve number is an experiential parameter applied as a portion of the hydrology calculation. It predicts the direct runoff and infiltration from surplus rainfall. Areas of low CN point to absorption, evaporation, surface storage, and transpiration processes [59]. The higher values of CN point to impervious areas leading to high runoff potentials. This variation based on slope, soil type, land-cover units, vegetation potency, and moisture content [60].

3.4. Rainfall–Runoff Modeling

Rainfall–runoff modeling was done using the package HEC-HMS (Hydrologic Engineering Center-Hydrologic Modeling Systems); it was established to simulate the processes of rainfall–runoff into watershed systems [61]. It has flexible options for assessing the penetration losses and hydrograph parameterizations [62].

Rainfall–runoff modeling uses various datasets such as DEM, land-use, soil type, and meteorological data. The soil conservation service curve number (SCS-CN) method was utilized. It calculates stream volume flow and create the hydrographs at the outlet of the main basin and sub-basins. This technique uses Equations (3)–(6) as follows:

$$\mathrm{CNw} = \frac{\Sigma \mathrm{CNi} * \mathrm{Ai}}{\mathrm{At}} \tag{3}$$

$$S = \left(\frac{100}{\mathrm{CNw}}\right) - 10 \tag{4}$$

$$Q = \frac{(p-0.25)^2}{(p+0.8S)} for\ Q > 0.2S : else\ Q = 0 \tag{5}$$

$$\mathrm{Ia} = 0.2\mathrm{S} \tag{6}$$

where $\mathrm{CN_w}$ is the weight of CN, $\mathrm{CN_i}$ is the CN of the same value in a sub-basin, $\mathrm{A_i}$ the area of $\mathrm{CN_i}$ in a sub-basin ($\mathrm{km^2}$), and $\mathrm{A_t}$ the total area of the sub-basin ($\mathrm{km^2}$). While S is the potential maximum soil moisture retention depth, $\mathrm{I_a}$ is the initial abstraction loss depth. Q is the direct runoff depth over the entire sub-basin for any return period, and P is the precipitation depth for 24 h duration storm for any return period at the same sub-basin. Moreover, the time of concentration, lag time, time to peak, and the maximum of the discharge parameters are assessed by using Equations (7) [63] and (8) [64] as follows:

$$\mathrm{T_c} = \frac{5}{3} + \mathrm{TL} \tag{7}$$

where $\mathrm{T_c}$ is the time of concentration (h) of any sub-basin, and TL is the lag time (h) for the same sub-basin.

$$\mathrm{T_p} = \frac{\Delta\mathrm{D}}{2} + \mathrm{TL} \tag{8}$$

where $\mathrm{T_p}$ is the time to peak, and ΔD is the duration time for excess rainfall (h).

3.5. Mapping of the Suitable Potential Sites for RWH

The used methods for determine the suitable locations of RWH are based on GIS, RS, and variables techniques. The analytical hierarchical process (AHP) technique was used, and the professional knowledge of six experts was utilized (Table 1) and Appendix B, Figure A1). It is one of the best-known and most commonly used multicriteria decision analysis (MCDA) methods [65–67]. Although this method needs a lot of metrological, morphometric, and land-use information, and it has a difficult validation process, it is a significant method, since a different construction may lead to a diverse final ranking [68–70]. It chooses the required criteria by ranking the factors and the qualitative and quantitative parameters [71]. It gives a framework, that can handle diverse opinions on determining the elements of a decision and arrange the elements into a hierarchical construction [72]. AHP has the advantage of permitting a hierarchical structure of the criteria, which provides users with a better focus on specific criteria and sub-criteria when allocating the weights. Furthermore, it aids decision-makers in finding the one that best suits their needs and their understanding of the problem, whereas it decreases bias in the decision-making procedure and provides group decision creation through agreement, utilizing the symmetrical mean of the separate decisions. The integration of AHP with GIS gives an efficient and user-friendly way of solving complex problems [60].

Table 1. Profiles of the experts.

Stakeholder Group	ID	Role	Division	Experience (Year)
Universities (UN)	E1	Assistant Lecturer	Hydrogeology	11
	E2	Professor	Hydrogeology	31
	E3	Professor	Meteorology	28
	E4	Professor	Environment	30
Water Research Center	E5	Associate Professor	Structural Engineering	25
Universities (UN)	E6	Professor	Soil	29

The land-cover, average of annual max 24 h rainfall, slope, stream order, and lineaments density were selected to determine suitable locations for RWH. The different data categories were reclassified into classes, and each class was given a definite rank that will impact RWH. The relative significance of different criteria are defined [69,73,74].

The rating rank is assigned to each layer based on the strength of significance [75] (Appendix A, Table A7) for each criteria. The pairwise comparison diagonal matrix was constructed. Then the relative weights were computed by standardizing any rows and columns for pairwise comparison diagonal matrices. However, a division of each component in each column is calculated by the summation of that column. The eigenvectors of these matrices are calculated by obtaining the mean of the normalizing matrix. Furthermore, the eigenvector of the normalizing matrices is equal to the weight values of every criterion. The pairwise comparison matrix is utilized in the description of weights for each criterion. The principal eigenvector of the pairwise comparison matrix is determined to give a good fit to the weight set. However, values of weight are absolute numbers ranging from zero to one. Utilizing a weighted linear combination shows that the sum of weights is equal to one.

The final mapping of suitable locations for RWH was delineated by establishing the AHP-GIS multi-criteria model, wherein the overlaying of the reclassified weighted raster was done. This criterion divided the raster into five classes; excellent, very good, moderate, poor, and unsuitable for RWH.

4. Results and Discussion

4.1. Morphometric Analysis

The study area was distinguished by composite and intertwining patterns that indicate the morphotectonic growth of the drainage basins. It was divided into fifteen sub-basins (Figure 3A). The morphometric analysis was classified into three morphometric attributes: linear, areal, and relief characteristics.

4.1.1. Linear Characteristics

The stream orders (U) are the 9th and 7th of the main basin and its sub-basins, respectively (Figure 3B). The high stream orders are related to the large areas and high discharge of stream flow. The stream number (Nu) for the main basin is 162,577, while the values for the 7th order sub-basins ranged from 2517 to 12,072 (sub-basins No. 4 and 10, respectively), with an average of 6294 and a standard deviation of 3041 (Table 2 and Appendix C, Table A8). The Nu of each order forms an inverse geometric sequence with order number and a direct relation with the basin size (Appendix C, Table A8). The high stream number value of sub-basin No. 10 referred to the small permeability and infiltration of the ground surface. Moreover, the different geological structures in each sub-basin are the main reason for the unequal stream number in each order.

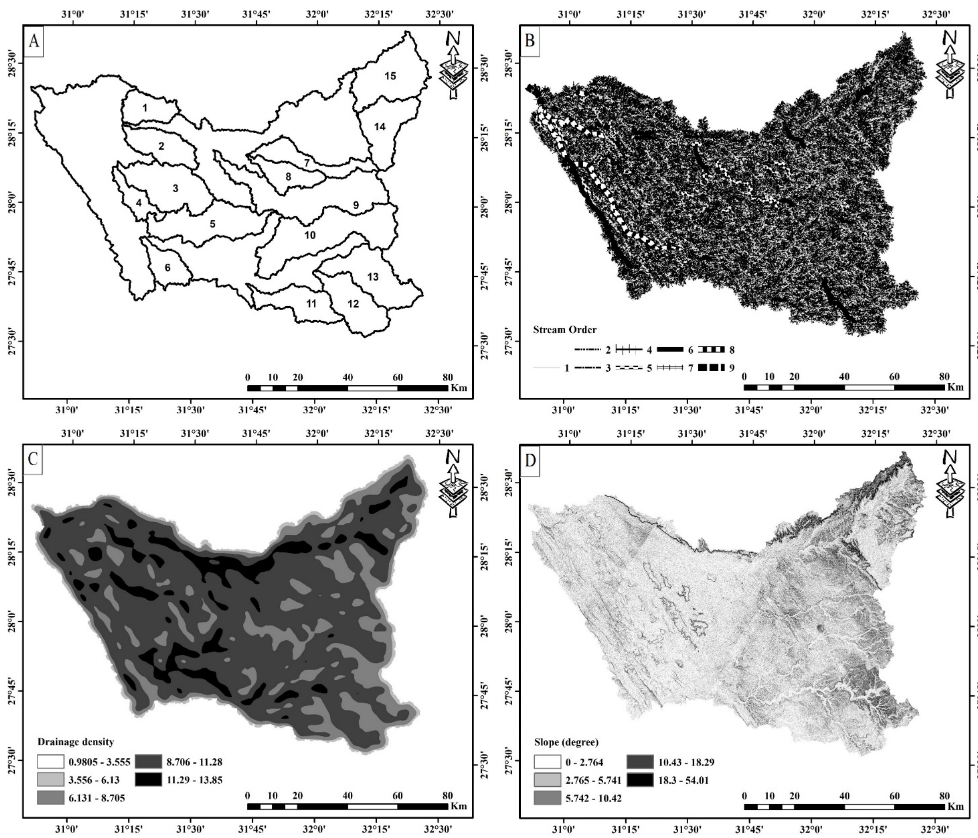

Figure 3. (**A**) Sub-basin number l; (**B**) stream order; (**C**) drainage density; (**D**) slope (degree).

Table 2. Descriptive statistics of the linear characteristics for 15 sub-basins in study area.

Parameters	Minimum	Maximum	Mean	Std. Deviation
Stream number (Nu)	2517	12,072	6294.53	3041.13
Stream length (Lu) in km	836.82	3818.30	2029.51	952.60
Mean bifurcation ratio (MRb)	3.70	8.98	4.50	1.27
Weighted mean bifurcation ratio (WMRb)	3.55	5.72	4.50	0.64
Basin length (Lb) in km	23.80	73.56	41.87	13.82
Length of overland flow (Lg) in km	2.30	2.66	2.49	0.10

The stream total length (Lu) for the main basin is 52,577 km, whereas, the values for the 7th order sub-basins ranged from 837 to 3818 km (sub-basins No. 4 and 10, respectively), with an average of 2029 km and standard deviation 952 (Table 2 and Appendix C, Table A8). The differences in the wadi length in these sub-basins are due to the variation of topography and geological structures that exist in these areas.

The value of the weighed mean bifurcation ratios (WMRb) for the main basin was 4.35 while the values for the 7th order sub-basin ranged from 3.55 to 5.72 (sub-basins No. 5 and 13, respectively), with a mean of 4.50 and a standard deviation of 0.64. Both the MRb (mean bifurcation ratio) and WMRb for the main basin and its sub-basins are >3 (Table 2 and Appendix C, Table A9). The high values of Rb indicate high mountainous areas and an elongated basin shape with low flooding potentialities. The small Rb value of the 7th order sub-basins indicate a circular basin shape with rapid hydrographic high peak flooding. These results can be explained by the sub-basins No. 12, 13, 14, and 15, which are more vulnerable to flooding (Appendix C, Table A9). The length of the main basin was 178 km, and the 7th order sub-basins length ranged from 24 to 74 km (sub-basins No. 1 and 9, respectively), with an average value of 42 km and a standard deviation of 13.82 (Table 2 and Appendix C, Table A9). The travel time of flood in sub-basin No. 9 is greater than in sub-basin No. 1, where the sub-basin No. 9 has good priorities for groundwater recharge (Appendix C, Table A9). The length of overland flow (Lg) indicates the flow length of the surface water before it reaches the specified channel of the main basin; it is 2.47 km for the mean basin, whereas, for the 7th order sub-basins, it ranged from 2.30 to 2.66 km (Sub-basins No. 13 and 6, respectively), with a mean value of 2.49 and a standard deviation of 0.10 (Table 2 and Appendix C, Table A9). The low values of Lg refer to a gentle slope with a longer flow path and more vulnerability to flash flooding (Appendix C, Table A9).

4.1.2. Areal Characteristics

The main basin area is 10,646 km^2, while the areas of the 7th order sub-basins range from 159 to 789 km^2 (sub-basins No. 4 and 10, respectively), with an average of 411 km^2 and a standard deviation of 198 (Table 3 and Appendix C, Table A10). The sub-basins are classified according to Horton (1945) into the category of large basins with an area >100 km^2, indicating the accumulation of a large amount of surface water.

Table 3. Descriptive statistics of the areal and relief characteristics of the main basin and its sub-basins.

Parameters	Minimum	Maximum	Mean	Std. Deviation
Basin area (A) in km^2	159.01	789.01	411.32	198.15
Basin perimeter (P) in km	90.08	258.93	144.00	48.81
Drainage density (Dd) in (km/km^2)	4.60	5.30	4.97	0.21
Stream frequency (Fs)	13.95	16.65	15.35	0.75
Texture ratio (T) in (km^{-1})	24.35	55.72	42.32	9.61
Relief ratio (Rh)	0.0046	0.0171	0.0084	0.0033
Basin slope (BS)	0.0406	0.1145	0.0620	0.0220

The basin perimeter (P) of the main basin is 808 km, whereas, the values for the 7th order sub-basin ranges from 90 to 259 km (sub-basin No. 6 and 9, respectively), with an average of 144 km and a standard deviation 49 (Table 3 and Appendix C, Table A10).

The drainage density (Dd) value of the main basin is 4.94 km/km^2, while the values of the 7th order sub-basins ranged from 4.60 to 5.30 km/km^2 (sub-basins No. 13 and 6, respectively), with a mean of 4.97 and a standard deviation of 0.21 (Table 3 and Appendix C, Table A10). The geological structure controls the areal distribution of drainage density in these sub-basins (Figure 3c). The high values of drainage density indicated high runoff potentialities, whereas, the low values indicate fractured rocks cover the ground surface. The high values of Dd for sub-basins No. 1–6 and 14 refer to impermeable rocks and, in some localities, sporadic vegetation (Appendix C, Table A10), while the low values of Dd refers to permeable rocks and soils with a low relief. Therefore, sub-basins with low Dd values could be good sites for groundwater recharge, while sub-basins with high values can form larger surface runoff.

The stream frequency (Fs) for the main basin is 15.27 km^{-2}, while the values for the 7th order sub-basins ranged from 13.95 to 16.65 km (sub-basins 13 and 5, respectively), with an average of 15.35 and a standard deviation of 0.75 (Table 3 and Appendix C, Table A10). The stream frequency is directly associated with lithological features; the basins with structural hills have high values of Fs and low values with alluvial deposits. Most of these sub-basins are distinguished by impermeable rocky areas with a low penetration capacity and a high vulnerability to flashflood.

The texture ratio (Rt) value of the main basin is 201 km^{-1}, while the values for the 7th order sub-basins range from 24 to 55 km^{-1} (sub-basin No. 4 and 10, respectively), with a mean of 43 km^{-1} and a standard deviation of 9.61 (Table 3 and Appendix C, Table A10). Sub-basins with lower values of Rt refer to plain basins with slight slopes [76,77], and these sub-basins have proper locations for groundwater recharge, such as sub-basin No. 4 (Figure 3a).

4.1.3. Relief Characteristics

The relief ratio (Rh) of the main basin is 0.007, whereas, the values for the 7th order sub-basins range from 0.005 to 0.017 (sub-basins No. 4 and 15, respectively), with an average value of 0.008 and a standard deviation of 0.003 (Table 3 and Appendix C, Table A10). The sub-basin No. 15 is like to experience large-scale flooding, and its high Rh value is directly related to flooding and contrary to the time of concentration. This can be explained by the presence of large areas of high-relief impervious limestone with a steep ground surface.

The slope value of the ground surface for the main basin is 0.056, while the values for the 7th order sub-basins range from 0.041 to 0.115 (sub-basins No. 5 and 15, respectively), with a mean of 0.062 and a standard deviation of 0.022 (Table 3, Appendix C, Table A10, and Figure 3d). The basins with gentle slopes are characterized by a long concentration time, little runoff, and small hydrograph peaks, such as sub-basins No. 2, 3, 4, 5, 6, and 11 (Figure 3d), whereas sub-basin 15 had a high slope value with a high amount of runoff and a shorter concentration time to the hydrograph peak. Therefore, sub-basin No. 15 could be more vulnerable to flooding events compared to other sub-basins.

Most of the sub-basins have a dendritic drainage pattern, reflecting little infiltration and extreme runoff events, particularly in the highly terrain areas. The main trend of the extracted liniments from Landsat image analysis is NW–SE, which is comparable with the Red Sea trend (Figure 4A,B).

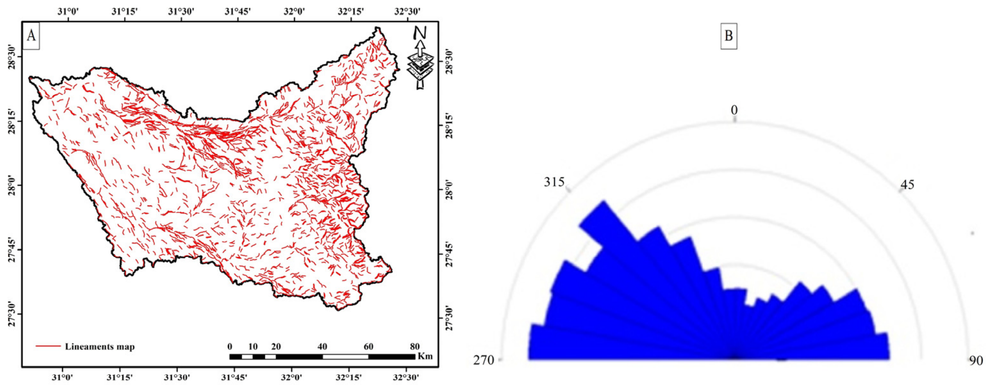

Figure 4. (**A**) Lineament map; (**B**) Rose diagram for lineaments.

4.2. Flashflood Hazard Assessment

The morphometric ranking method was used to define the degree of flashflood hazards. It was carried out by an analysis of different scores of morphometric variables (Table 4). The 7th order sub-basins were categorized according to flooding vulnerability by different relative hazard degrees, which are divided into five classes: extremely high, high, moderate, low, and very low (Figure 5). The low-flooding-susceptibility area is in sub-basin No. 4. On the other hand, sub-basins No. 15, 14, 10, 9, and 3 show extremely high scores, representing the most dangerous sub-basins.

The most hazardous and threatening sub-basins are located in the upper part of the basin. The potential for vulnerability to flooding is high due to high slopes and a lack of stream meanders. Several solutions must be carried out to protect the area. Three and six sub-basins have a moderate and low-flooding-susceptibility degree, respectively.

Table 4. Hazard degrees of the effective parameters.

Basin No	Relative Hazard Degrees of the Effective Parameters														Basin Hazard Degree
	A	Dd	Fs	Rr	SI	Rn	Rt	Ish	BS	ΣN	ΣL	Lg	WMRb	MRb	
1	1.41	3.85	3.22	3.74	3.02	5.00	2.88	1.90	2.60	2.13	1.39	1.41	2.26	4.92	3
2	1.91	3.77	2.88	3.89	1.57	3.10	1.47	1.58	3.09	1.03	1.88	1.96	2.11	4.71	2
3	3.24	4.77	4.80	4.29	1.33	3.61	1.54	2.04	5.00	1.36	3.49	3.44	1.71	4.51	4
4	1.00	4.58	3.78	4.68	1.00	2.23	1.00	1.01	1.00	1.04	1.00	1.00	1.32	5.00	1
5	3.44	5.00	5.00	3.98	1.37	2.30	1.42	2.40	3.75	1.00	3.73	3.62	2.02	1.00	3
6	1.30	3.97	3.57	5.00	1.25	3.49	1.07	1.00	2.48	1.07	1.30	1.35	1.00	4.93	2
7	1.77	2.85	2.80	2.39	1.81	1.00	2.68	3.90	1.33	2.50	1.73	1.70	3.61	4.67	2
8	1.41	4.02	4.01	2.21	1.79	2.38	2.42	2.18	2.27	2.61	1.44	1.32	3.79	4.73	2
9	4.97	3.25	2.97	2.38	1.55	1.64	2.21	4.54	3.79	2.40	4.96	4.98	3.62	4.20	4
10	5.00	3.01	3.00	2.31	1.74	2.35	2.22	3.89	4.84	2.21	5.00	5.00	3.69	4.29	4
11	2.02	2.66	3.32	2.66	1.53	2.17	1.64	2.01	2.66	1.28	2.02	1.98	3.34	4.67	2
12	2.46	1.93	2.31	1.73	1.54	3.48	1.90	1.94	4.02	2.04	2.36	2.35	4.27	4.56	2
13	3.10	1.00	1.00	1.00	1.68	3.05	2.35	2.71	3.69	4.37	2.81	2.91	5.00	4.54	3
14	2.49	2.37	1.80	3.25	5.00	4.70	3.55	3.10	4.07	2.33	2.34	2.52	2.75	4.68	4
15	3.50	1.63	1.60	2.25	3.60	4.42	5.00	5.00	4.77	5.00	3.27	3.46	3.75	4.50	5

Sub-basin area (A), drainage density (Dd), stream frequency (Fs), relief ratio (Rr), slope index (SI), ruggedness number (Rn), texture ratio (Rt), shape index (Ish), basin slope (BS), total stream number (ΣN), total stream length (ΣL), length of overland flow (Lg), weighed mean bifurcation ratios (WMRb), mean bifurcation ratio (MRb).

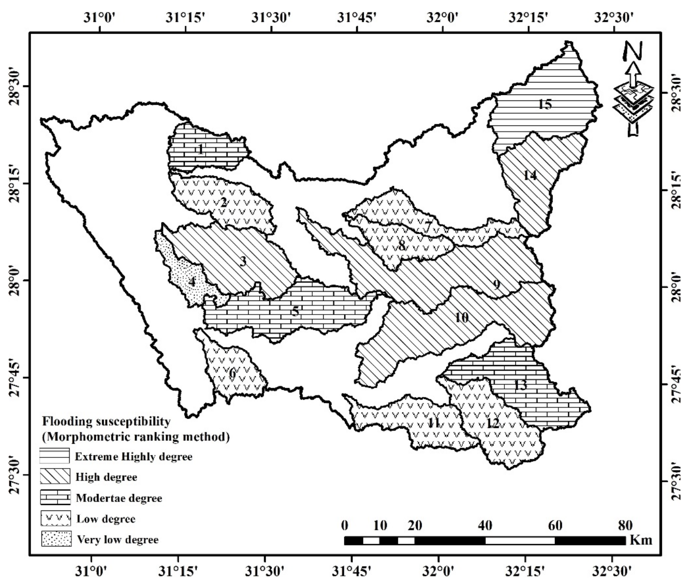

Figure 5. Flooding susceptibility: morphometric ranking method.

4.3. Rainfall–Runoff Modeling

Five hypothetical proposed storms were established for rainfall events with 5-, 10-, 25-, 50-, and 100-year return periods. The maximum 24 h rainfall data of the five return periods ranges from 1 to 55 mm/year (Appendix B, Figure A2). The appropriate curves between the return period and the historic 24 h rainfall depth was calculated with a confidence level of about 95% (Figure 6). The southeastern part of the study area is characterized by high rates of rainfall. Due to the prevalence of steep slopes in this area, rainwater harvesting is unfavorable. The central part of this basin is characterized by low rainfall rates, moderate runoff, and gentle slopes; therefore, potential sites for rainwater harvesting can be delineated (Figure 3d).

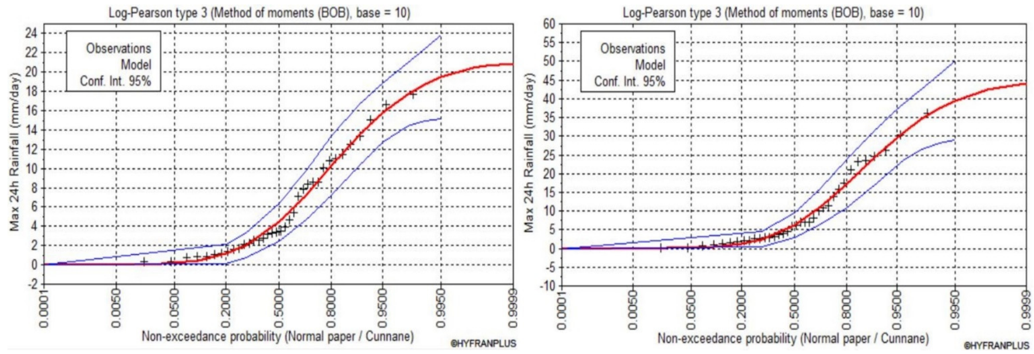

Figure 6. The maximum 24 h rainfall data for the temporal analysis of rainfall data.

The CN values of the different land-use classes vary between 55 and 89 (Appendix C, Table A11); they indicate vegetation, quarries, recent alluvium, weathered limestone, old alluvium, and massive limestone (Figure 7A). The CN values were validated using field observations and geological map. Also, band ratio (7/5, 3/2, 4/5), principal component analysis (1, 4, 3), and composite bands (7, 6, 2) were used in confirming this validation (Figure 7B–F).

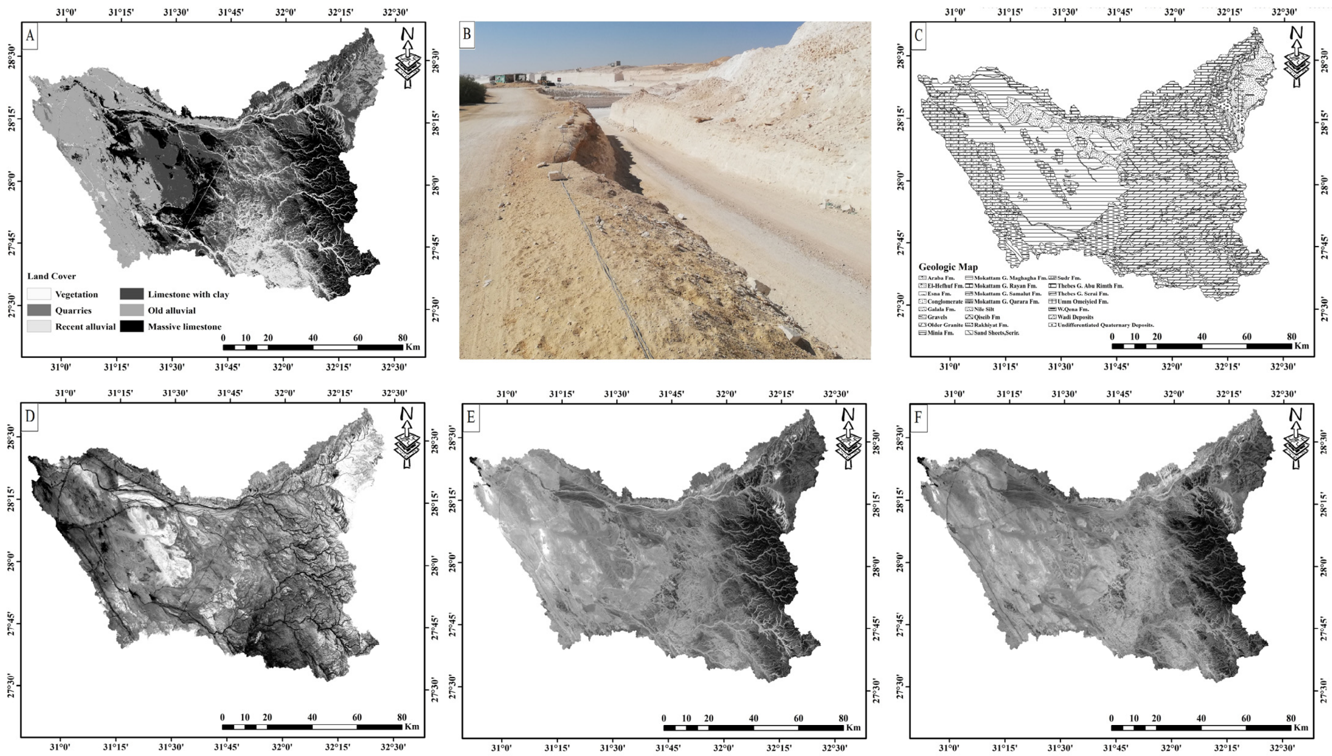

Figure 7. (**A**) Curve number map; (**B**) field plot; (**C**) geologic map; (**D**) band ratio (7/5, 3/2, 4/5); (**E**) principle component (1, 4, 3); (**F**) composite bands (7, 6, 2).

The different input factors of the constructed hydrological model were investigated. To simulate the hydrological probability, the SCS-CN method was utilized (Appendix C, Table A12). The hydrograph and peak discharge of each return period were calculated and assessed at the outlet of each sub-basin (Table 5 and Figure 8). The values of the flood peak increase with the increasing of return periods. The values of the peak discharge of sub-basin No. 15 are the greatest compared to the other sub-basins. It ranged from 40.5 to 201.5 m^3/s (5- and 100-year return periods, respectively). Sub-basin No. 4 presented the lowest values of peak discharge; it ranged from 1.8 to 4.3 m^3/s (5- and 100-year return periods, respectively).

Sub-basin No. 15 showed high vulnerability to flooding, as illustrated by morphometric ranking (Table 4). For the main basin, the value of peak runoff discharge ranged between 60.3 and 358.3 m^3/s, with a total volume of 102,478 m^3 and 60826.4 m^3 (5-year and 100-year periods, respectively), (Figure 9).

Table 5. Peak discharge of runoff values (m^3/s) for each sub-basin and each return period.

Basin No	**Return Period (Year)**				
	5	**10**	**25**	**50**	**100**
1	3.6	4.7	6	6.7	7.6
2	7.6	11.9	20	25.8	31.9
3	35	49.9	67.2	83.7	99.1
4	1.8	2.5	3.1	3.4	4.3
5	9.1	14.3	24.9	35.8	46.5
6	4.1	6.1	9.3	13.7	18.7
7	8.5	15.4	27.1	36.2	44.9
8	2.8	4.2	7.8	11.4	14.7
9	16.5	29.7	52	68.2	80.4
10	11.2	18.1	32.7	44.4	54.7
11	2.7	4.2	6.2	7.4	9.2
12	5.5	10.1	26.5	43.7	61.3
13	8.8	22.6	55.1	82.7	109.4
14	21.6	39.2	70.1	93.8	115
15	40.5	72.5	127.2	167.3	201.5
Main basin	60.3	95.9	188.4	273.7	358.3

The outcropped massive limestone rocks are highly affecting the hydrological setting. They decrease the rate of infiltration and increase runoff, therefore leading to high flooding events. Consequently, intensive rainfall storms can form high peak floods in short times, which can threaten urban areas and agricultural areas (Appendix A, Figure A3). Therefore, low dams are proposed at proper sites for protection. In areas covered with alluvium deposits and gentle slopes, water can be harvested to recharge groundwater or is used directly for domestic and agriculture purposes.

4.4. Multi-Criteria Decision Analysis for the Study Area

Five layers of information were used to assess flooding potentialities and in particular propose suitable locations for RWH. Six units of land-cover were extracted using a supervised analysis of Landsat-8 images (Figure 10A). These six units were classified into six classes; the hard massive and impervious unit took the high rate. The different land-cover units had different scores, which were relative to rock type, permeability, and vegetation cover: massive limestone, limestone with clay, quarries, old alluvial, recent alluvial, and vegetation (6, 5, 4, 3, 2, and 1, respectively), (Figure 10B and Appendix C, Table A12). The intensity of importance for land-cover ranged from 1 to 3, with a total value of 5.53 and an eigenvector of 0.21 (Tables 6 and 7). The average annual max 24 h rainfall was extracted from a historical data log (1979 to 2014). The max 24 h rainfall distribution was reclassified into five classes, wherein the high-intensity rainfall was taken as a high rate (Figure 10C,D and Appendix C Table A12). The intensity of importance for rainfall criteria with other criteria ranged from one to three, with a total of 5.67 and an eigenvector of 0.19 (Tables 6 and 7). Figure 10c shows the rainfall distribution in the study area, where the higher values are recorded in the upstream area to the east, where it is characterized by steep slopes with high run-off events, therefore making it unsuitable for RWH. DEM processing and analysis was used to extract the different slope classes (Figure 10E). The rating criteria reclassifies the slope into five classes, wherein the low-slope areas result in a high rate value (Figure 10F and Appendix C Table A12). The slope importance criteria relative to other variables ranged from 0.14 to 1, with a total of 2.01 and a high value of the eigenvector at 0.47 (Tables 6 and 7). Runoff flows very fast in steep areas in the upstream basin, whereas a slow flow was recorded in the gentle-slope areas in the downstream basin. The main stream order (U) is ninth (Figure 10G), and the order criteria rates and reclassified basin into nine classes, wherein the ninth class has a high rate (Figure 10H and Appendix C Table A12). The intensity of the importance value for stream order ranged from one to seven, with a total value of 17 and an eigenvector of 0.06 (Tables 6 and 7). The nominated best sites for RWH are close to the main stream; this has adequate economic feasibility because it reduces the cost of construction (dam No. 1 and 2), and it can also collect a large amount of rainwater. Lineament density was extracted from Landsat-8 image analysis (Figure 10I). The lineament density map was reclassified into five classes, wherein the high-density class has a high rate (Figure 10J and Appendix C Table A12). The lineaments importance criteria in relation to other variables ranged from 1 to 5, with a total of 13 and an eigenvector of 0.07 (Tables 6 and 7). The density of lineaments is an important factor in locating RWH sites; areas with high lineaments density are suitable for RWH, as it assists with rainwater infiltration to the groundwater.

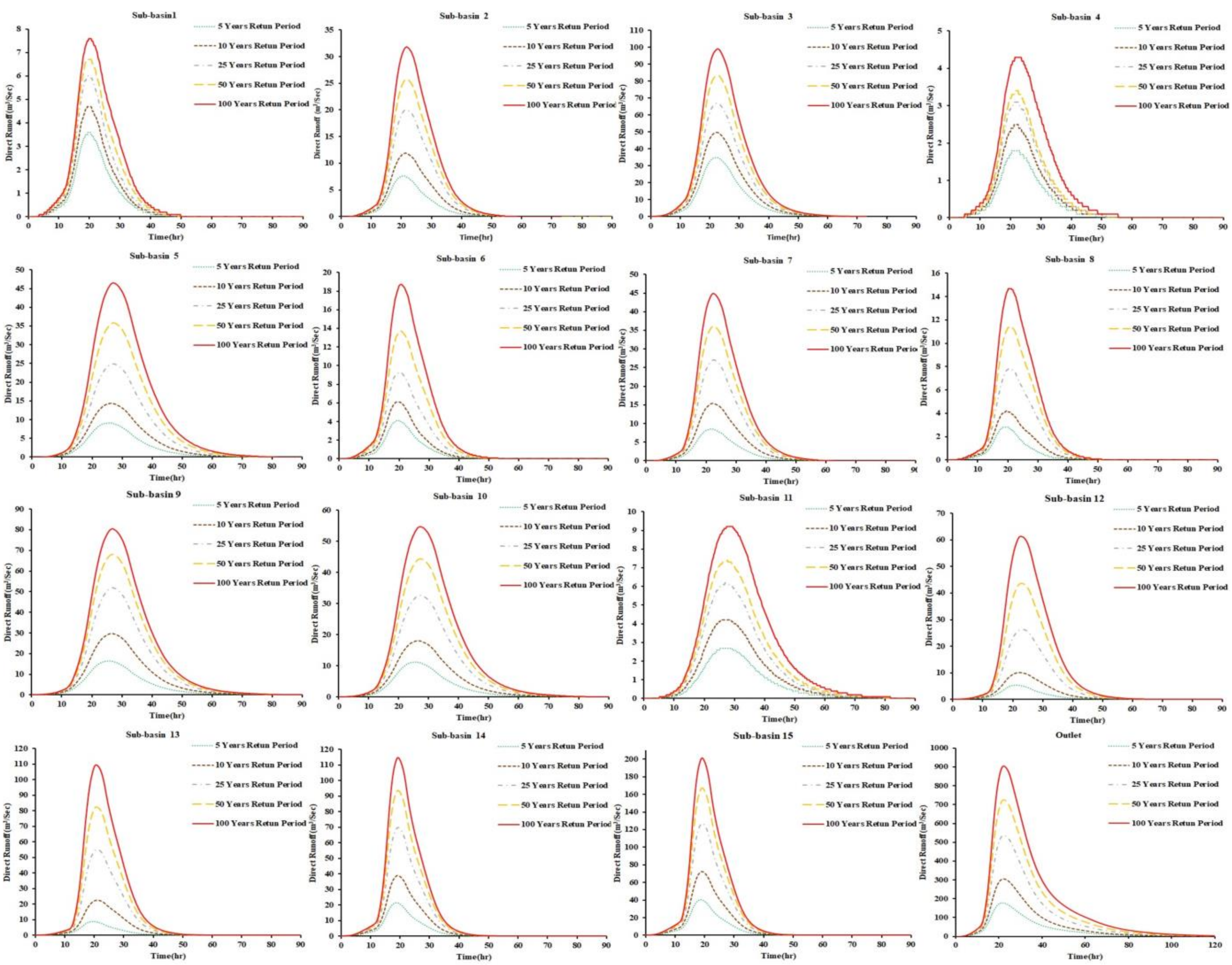

Figure 8. Hydrograph curves for each sub-basin and each return period.

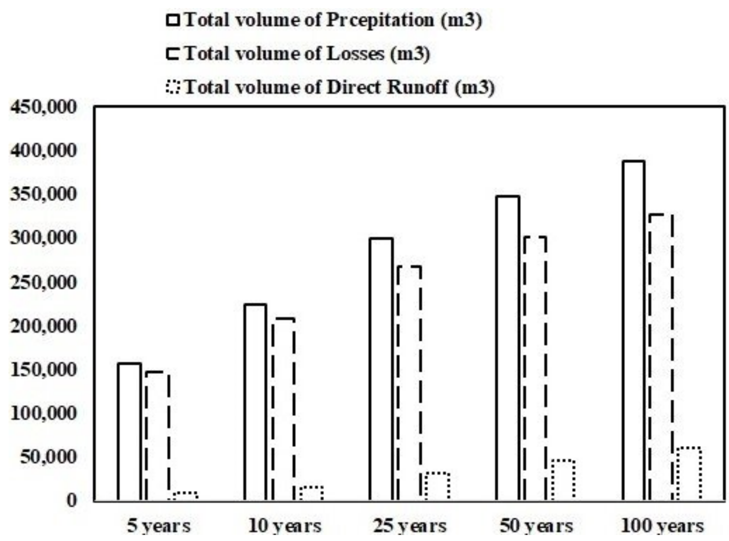

Figure 9. Histogram showing rainfall, runoff, and return period for the main basin.

Table 6. Comparison matrix for the criteria for suitable locations for RWH.

Criteria	Rainfall	Land Cover	Slope	Stream Order	Lineaments
Land cover	1	1	0.33	5	3
Rainfall	1	1	0.33	3	3
Slope	3	3	1	7	5
Stream order	0.33	0.2	0.14	1	1
Lineaments	0.33	0.33	0.2	1	1
Total	5.67	5.53	2.01	17	13

Table 7. Normalizing the columns of the RWH criteria to obtain the normalized matrix.

Criteria	Rainfall	Land Cover	Slope	Stream Order	Lineaments	Egin Vector
Land cover	0.18	0.18	0.16	0.29	0.23	0.21
Rainfall	0.18	0.18	0.16	0.18	0.23	0.19
Slope	0.53	0.54	0.50	0.41	0.38	0.47
Stream order	0.059	0.04	0.07	0.06	0.08	0.06
Lineaments	0.059	0.06	0.10	0.06	0.08	0.07
Total	1	1	1	1	1	1

Rainfall-Harvesting Map

The AHP multi-criteria method was used to determine the appropriate locations for rainwater harvesting. The RWH map was constructed by overlaying reclassified maps, which were selected by different criteria: land cover, average annual max 24 h rainfall, slope, stream order, and lineaments density (Figure 10). Each of these parameters had its relative weight according to the normalized matrix (Table 7).

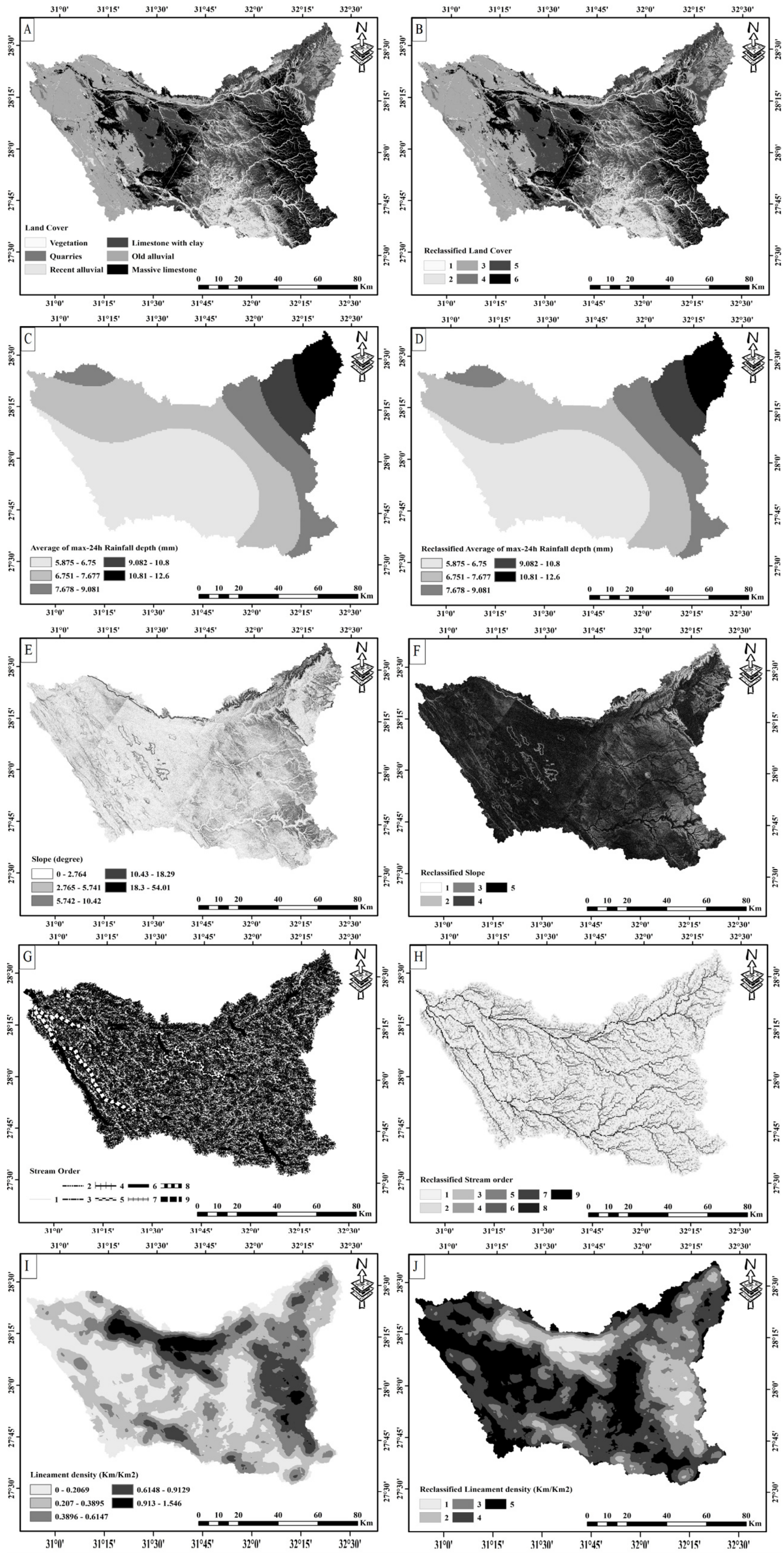

Figure 10. Criteria maps for the AHP of rainwater harvesting in the study area. (**A**) land cover; (**B**) reclassified land cover; (**C**) average of max 24 h rainfall depth (mm); (**D**) reclassified average of max 24 h rainfall depth (mm); (**E**) slope; (**F**) reclassified slope; (**G**) stream order; (**H**) reclassified stream order; (**I**) lineament density; (**J**) reclassified lineament density.

Most parts of the northeast and southeast region have a high value of rainfall; slopes and fine hydrological network. While the steep central parts of the basin are characterized by gentle slopes with little rainfall. However, there low rates of rainfall in this area, where the main stream passes through the central part of the basin. Therefore, these areas are suitable sites for rainwater harvesting (Figure 11). Low-potential sites for rainwater harvesting are distributed in different parts of the basin. They are affected by steep slopes with little rainfall compared with other criteria. The ground surface slope has great impact, more than other variables for delineating areas suitable for rainwater harvesting (Figure 3D). The highly suitable sites for rainfall harvesting cover 6708 km^2, while the moderate- and low-suitability zones cover 3620 km^2 and 319 km^2, respectively (Figure 11B). Ten sites have been proposed for dam construction to locate suitable dam reservoirs (Figure 11A); they are dependent mainly on topography, average rainfall rates, and the economic importance of the site. The values of peak discharge at dam No. 2 ranged from 44.0 to 288.5 m^3/s (5- and 100-year return periods, respectively). Dam No. 1 presents the minimum values of peak discharge; it ranged from 0.9 to 2.0 m^3/s (5- and 100-year return periods, respectively), (Table 8, Figure 12 and Appendix C, Tables A13 and A14).

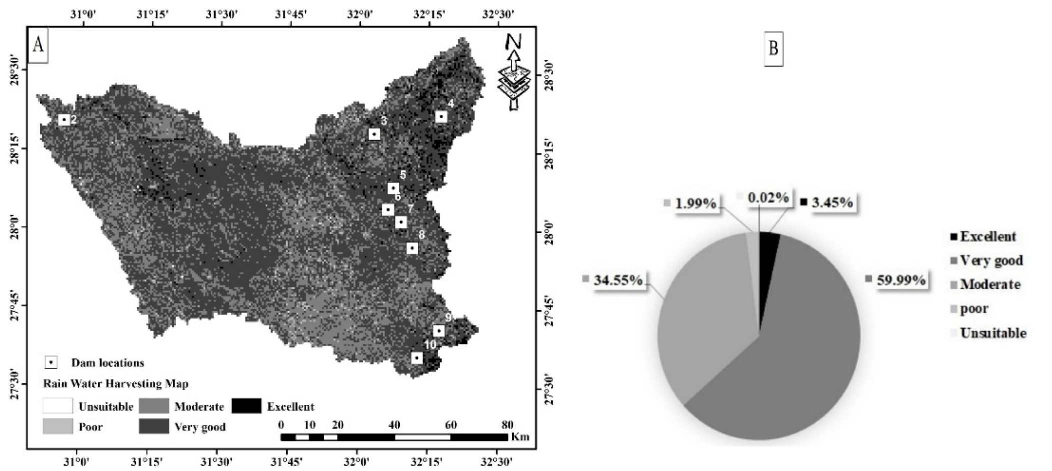

Figure 11. (**A**) Rainwater-harvesting map for the study area; (**B**) percentage of the area covered by different rainwater-harvesting suitability.

Table 8. Peak discharge of runoff values (m^3/s) for each dam and each return period.

Dam No	Return Period (Year)				
	5	**10**	**25**	**50**	**100**
1	0.90	1.20	1.60	1.80	2.00
2	44.00	84.60	164.70	229.00	288.50
3	4.00	6.20	9.50	11.90	14.10
4	5.70	8.80	14.80	19.70	23.80
5	1.60	2.30	3.10	3.50	3.90
6	17.30	24.70	32.80	37.90	41.90
7	5.20	7.50	9.80	11.40	12.60
8	3.10	4.70	6.00	6.90	7.60
9	2.30	4.00	6.90	9.00	11.00
10	11.40	18.90	29.00	36.40	43.20

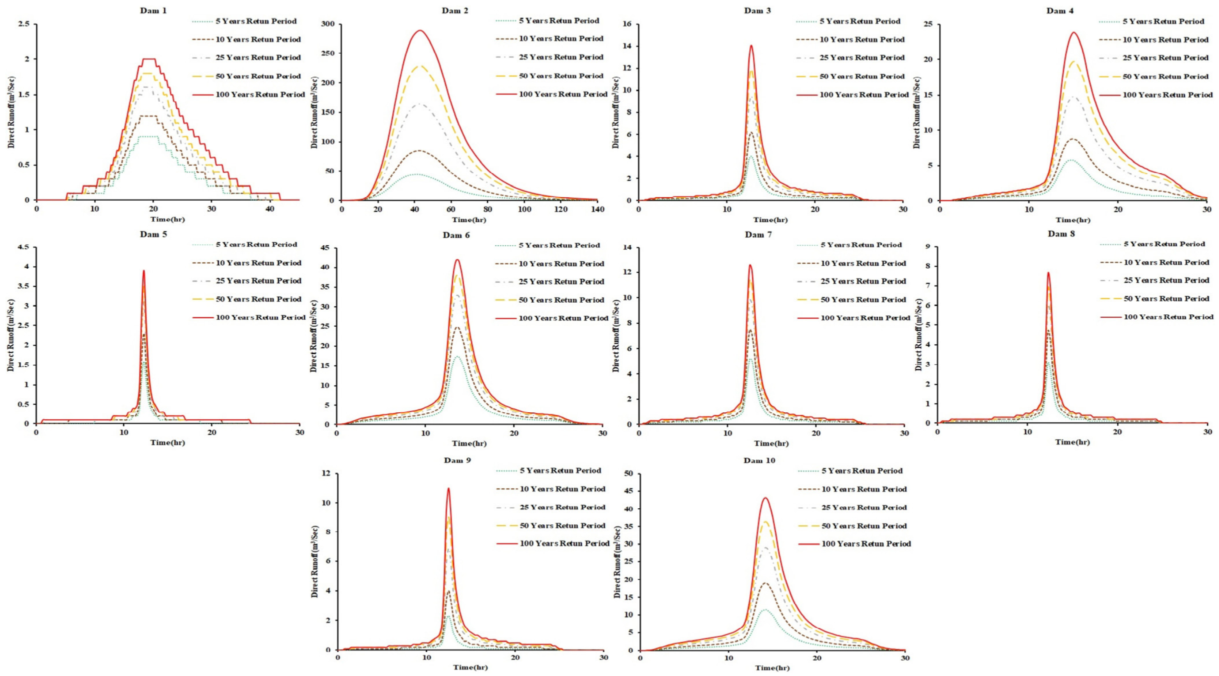

Figure 12. Hydrograph curves for each dam and each return period.

5. Conclusions

Predicting runoff events is a prodigious problem in ungauged arid areas, where the monitoring of flashfloods is a big challenge due to inadequate observational data, the absence of monitoring systems, and a lack of infrastructure. The peak discharge of flashfloods and RWH could be assessed by the integration of GIS, RS techniques, and hydrologic modeling. Dlimate change and the rising of water demands for drinking and agricultural and industrial purposes can increase the pressure on limited water resources. The study area was divided into fifteen sub-basins. Most of the sub-basins have a dendritic drainage pattern. The different morphometric parameters (linear, areal, and relief characteristics) were extracted. They show that the most hazardous and threatening sub-basins were located in the upstream zone of the basin (sub-basins No. 15, 14, 10, and 9). The vulnerability potential for flooding is high in upstream areas. The steep slopes, high drainage density and frequency, and the low degree of stream sinuosity are high relative to the possibility of flooding.

The hydrologic model shows that high rates of rainfall and steep slopes are present in the southeastern part of the study area. The high discharge peak is recorded in sub-basin No. 15 (40.5–201.5 m^3/s for 5- and 100-year return periods, respectively), while the low peak is in sub-basin No. 4 (1.8–4.3 m^3/s for 5- and 100-year return periods, respectively). For the main basin, the value of peak runoff discharge ranged between 60.3 and 358.3 m^3/s, with a total volume of 102,478 m^3 and 60,826.4 m^3 (5-year and 100-year periods, respectively). Low rainfall rates, moderate–high runoff, and gentle slopes were found in the central and downstream parts. Therefore, these areas are appropriate sites for rainwater harvesting. In central and downstream areas covered with alluvium deposits and having gentle slopes, water can be harvested to replenish groundwater or used directly for domestic and agriculture purposes. An analytic hierarchy process (AHP) was applied for mapping the best sites to RWH. This criterion used land-cover, average annual max 24 h rainfall, slope, stream order, and lineaments density. The ground surface slope had a great impact, more than other variables for delineating suitable areas for rainwater harvesting. About 4% of the basin area had a very high potentialities for RWH, while 59% of the basin area had high RWH suitability. Several solutions are recommended to be carried out to protect the area against flashflood hazards. In the study area, ten low dam sites were proposed to impact flooding vulnerability and rainwater-harvesting potentialities. This approach can be used successfully to delineate suitable sites for rainwater harvesting for proper adaptation practice against climate change in similar arid conditions.

Author Contributions: Conceptualization, M.E.A.; Methodology, H.M. and M.E.A.; Software, H.M.; Validation, M.E.A.; Data curation, A.E.-K.; Writing—original draft preparation, H.M.; Writing—review and editing, M.E.A. and A.E.-K.; Supervisor, M.E.A. All authors have read and agreed to the published version of the manuscript.

Funding: This research received no external funding.

Institutional Review Board Statement: Not applicable.

Informed Consent Statement: Not applicable.

Data Availability Statement: Please check: https://power.larc.nasa.gov/data-access-viewer/ (accessed on 14 February 2022).

Acknowledgments: The authors would like to thank Geology Department, Mansoura University for logistical support. Also, they sincerely appreciate the financial support of the Sustainability Journal to publish this paper.

Conflicts of Interest: The authors declare no conflict of interest.

Appendix A

Table A1. Maximum and minimum temperature trend.

ID	Lon(x)	Lat(y)	Begin	End	Max-Trend		Min-Trend	
					LinTrend/Decade	p-Value of t-Test	LinTrend/Decade	p-Value of t-Test
N276313	31.25	27.632	1979	2014	0.270	0.018	0.210	0.037
N276322	32.188	27.632	1979	2014	0.280	0.024	0.120	0.255
N276325	32.5	27.632	1979	2014	0.370	0.002	0.160	0.075
N279309	30.938	27.945	1979	2014	0.300	0.005	0.250	0.010
N279313	31.25	27.945	1979	2014	0.270	0.015	0.180	0.075
N279316	31.563	27.945	1979	2014	0.320	0.007	0.130	0.217
N279319	31.875	27.945	1979	2014	0.370	0.002	0.130	0.212
N279322	32.188	27.945	1979	2014	0.390	0.001	0.150	0.112
N283309	30.938	28.257	1979	2014	0.340	0.001	0.420	0.001
N283313	31.25	28.257	1979	2014	0.290	0.010	0.150	0.129
N283316	31.563	28.257	1979	2014	0.310	0.008	0.040	0.735
N283319	31.875	28.257	1979	2014	0.390	0.001	0.080	0.442
N283322	32.188	28.257	1979	2014	0.430	0.000	0.040	0.686
N286309	30.938	28.569	1979	2014	0.380	0.000	0.450	0.001
N286313	31.25	28.569	1979	2014	0.280	0.010	0.100	0.317
N286316	31.563	28.569	1979	2014	0.300	0.010	−0.050	0.660
N286319	31.875	28.569	1979	2014	0.420	0.001	0.040	0.723
N286322	32.188	28.569	1979	2014	0.310	0.011	−0.170	0.156
N289309	30.94	28.88	1979	2014	0.340	0.001	0.360	0.002
N289313	31.25	28.88	1979	2014	0.310	0.004	−0.030	0.788
N289316	31.56	28.88	1979	2014	0.410	0.000	−0.010	0.923
N289319	31.88	28.88	1979	2014	0.630	0.000	0.150	0.139
N292313	31.250	29.193	1979	2014	0.390	0.000	0.050	0.566
N292316	31.563	29.193	1979	2014	0.360	0.001	0.190	0.028
N292319	31.875	29.193	1979	2014	0.400	0.000	0.190	0.026
N295313	31.250	29.506	1979	2014	0.460	0.000	0.180	0.022
N295316	31.563	29.506	1979	2014	0.440	0.000	0.280	0.002
N295319	31.875	29.506	1979	2014	0.340	0.002	0.170	0.041

Table A2. Precipitation and relative humidity trend.

ID	Lon(x)	Lat(y)	Begin	End	Precipitation Trend		Relative Humidity Trend	
					LinTrend/Decade	*p*-Value of *t*-Test	LinTrend/Decade	*p*-Value of *t*-Test
N276313	31.25	27.632	1979	2014	−8.520	0.015	0.000	0.000
N276322	32.188	27.632	1979	2014	−8.080	0.023	−0.010	0.018
N276325	32.5	27.632	1979	2014	−7.110	0.025	0.000	0.092
N279309	30.938	27.945	1979	2014	−6.880	0.039	0.000	0.000
N279313	31.25	27.945	1979	2014	−5.730	0.068	0.000	0.000
N279316	31.563	27.945	1979	2014	−5.270	0.079	0.000	0.198
N279319	31.875	27.945	1979	2014	−5.100	0.085	−0.010	0.054
N279322	32.188	27.945	1979	2014	−5.100	0.090	0.000	0.000
N283309	30.938	28.257	1979	2014	−5.080	0.107	0.000	0.000
N283313	31.25	28.257	1979	2014	−4.790	0.117	0.000	0.166
N283316	31.563	28.257	1979	2014	−4.690	0.158	0.000	0.000
N283319	31.875	28.257	1979	2014	−4.590	0.191	0.000	0.000
N283322	32.188	28.257	1979	2014	−3.990	0.205	−0.010	0.295
N286309	30.938	28.569	1979	2014	−3.900	0.209	−0.010	0.213
N286313	31.25	28.569	1979	2014	−3.900	0.215	0.010	0.147
N286316	31.563	28.569	1979	2014	−3.620	0.216	0.000	0.166
N286319	31.875	28.569	1979	2014	−3.530	0.239	0.000	0.638
N286322	32.188	28.569	1979	2014	−3.450	0.266	−0.010	0.175
N289309	30.94	28.88	1979	2014	−3.300	0.269	−0.010	0.444
N289313	31.25	28.88	1979	2014	−3.210	0.308	0.010	0.063
N289316	31.56	28.88	1979	2014	−2.500	0.360	0.000	0.498
N289319	31.88	28.88	1979	2014	−2.410	0.361	−0.010	0.291
N292313	31.250	29.193	1979	2014	−2.230	0.384	0.000	0.166
N292316	31.563	29.193	1979	2014	−2.220	0.387	0.000	0.166
N292319	31.875	29.193	1979	2014	−2.180	0.473	−0.010	0.152
N295313	31.250	29.506	1979	2014	−1.740	0.519	−0.010	0.161
N295316	31.563	29.506	1979	2014	−1.510	0.574	−0.020	0.059
N295319	31.875	29.506	1979	2014	−0.740	0.773	−0.010	0.072

Table A3. Sunshine and wind trend.

ID	Lon(x)	Lat(y)	Begin	End	Sunshine Trend		Wind Trend	
					LinTrend/Decade	*p*-Value of *t*-Test	Amount/Decade	Sig. Level
N276313	31.25	27.632	1979	2014	0.180	0.005	−0.030	0.084
N276322	32.188	27.632	1979	2014	0.190	0.004	−0.060	0.005
N276325	32.5	27.632	1979	2014	0.200	0.003	−0.090	0.002
N279309	30.938	27.945	1979	2014	0.230	0.001	−0.020	0.088
N279313	31.25	27.945	1979	2014	0.180	0.004	−0.020	0.048
N279316	31.563	27.945	1979	2014	0.150	0.013	−0.050	0.004
N279319	31.875	27.945	1979	2014	0.150	0.014	−0.070	0.000
N279322	32.188	27.945	1979	2014	0.210	0.003	−0.070	0.002
N283309	30.938	28.257	1979	2014	0.240	0.001	−0.010	0.387
N283313	31.25	28.257	1979	2014	0.200	0.004	−0.010	0.323
N283316	31.563	28.257	1979	2014	0.170	0.009	−0.040	0.006
N283319	31.875	28.257	1979	2014	0.170	0.008	−0.060	0.002
N283322	32.188	28.257	1979	2014	0.220	0.003	−0.070	0.001
N286309	30.938	28.569	1979	2014	0.240	0.001	0.010	0.528
N286313	31.25	28.569	1979	2014	0.180	0.005	−0.010	0.213
N286316	31.563	28.569	1979	2014	0.160	0.009	−0.050	0.001

Table A3. *Cont.*

ID	Lon(x)	Lat(y)	Begin	End	Sunshine Trend		Wind Trend	
					LinTrend/Decade	*p*-Value of *t*-Test	Amount/Decade	Sig. Level
N286319	31.875	28.569	1979	2014	0.190	0.005	−0.050	0.001
N286322	32.188	28.569	1979	2014	0.240	0.002	−0.080	0.000
N289309	30.94	28.88	1979	2014	0.240	0.001	0.000	0.883
N289313	31.25	28.88	1979	2014	0.170	0.007	−0.020	0.063
N289316	31.56	28.88	1979	2014	0.170	0.011	−0.060	0.001
N289319	31.88	28.88	1979	2014	0.210	0.003	−0.060	0.000
N292313	31.250	29.193	1979	2014	0.200	0.003	−0.020	0.095
N292316	31.563	29.193	1979	2014	0.210	0.002	−0.040	0.005
N292319	31.875	29.193	1979	2014	0.240	0.002	−0.060	0.000
N295313	31.250	29.506	1979	2014	0.250	0.001	−0.010	0.281
N295316	31.563	29.506	1979	2014	0.250	0.001	−0.030	0.004
N295319	31.875	29.506	1979	2014	0.260	0.001	−0.040	0.004

Table A4. Linear aspects of the drainage watershed.

Morphometric Parameters	Formula	Reference
Stream order (U)	Hierarchical order	[1]
Stream Length (LU) km	The total length of the stream of order (u)	[2]
Bifurcation Ratio (Rb)	Rb = Nu/Nu + 1, where Nu = number of stream segments in order (u), Nu + 1 = number of segments of the next higher order	[3]
Mean bifurcation ratio (MRb)	The average of bifurcation ratios of all orders	[1]
Weighted Mean bifurcation ratio (WMRb)	$WMRb = \frac{\Sigma\,(Nu/Nu+1)/\times(Nu+Nu+1)}{N}$ Where Nu = number of stream segments in order (u), Nu+1 = number of segments of the next higher order, N = total number of streams involved	[4]
Basin length (Lb) km	Extracted by the spatial analyst tool in ArcMap	[3]
Length of overland flow (Lg) km	Lg = 1/2 Dd, where Dd = drainage density	[2]

Table A5. Areal aspects of the drainage watershed.

Morphometric Parameters	Formula	Reference
Basin area (A) km^2	Extracted by the spatial analyst tool in ArcMap	[3]
Basin perimeter (P) km	Extracted by the spatial analyst tool in ArcMap	[3]
Drainage density (Dd) km/km^2	Dd = L/A, where L = total length of the stream, A = area of the basin	[5]
Stream frequency (Fs) km^{-2}	Fs = ΣN/A, where ΣN = total number of stream segments in all orders, A = area of the basin	[5]
Texture ratio (T)	T = ΣN/P, where ΣN = Total number of stream segments in all orders, P = perimeter of the basin	[2]
Shape index (Ish)	$Ish = 1.27 \times R_f$ (R_f form factor)	[2,3]

Table A6. Relief aspects of the drainage watershed.

Morphometric Parameters	Formula	Reference
Relief ratio (Rh)	Rh = Bh/Lb, where Bh = basin relief, Lb = basin length	[3]
Basin slope (BS)	Extracted by (WMS software)	[2]
Drainage patterns (Dp)	Stream network using GIS software analysis	[5]
Ruggedness Number (Rn)	Rn = Bh × Dd, where Bh = basin relief, Dd = drainage density	[6]
Slope index (SI)	SI = Bh/Lms, where Bh = basin relief, Lms = length of main stream	[7]

Table A7. Scale for pair-wise comparisons [8].

Intensity of Importance	Definition	Description
1	Equally important	Two factors contribute equally to the objective.
3	Moderately more important	Experience and judgment slightly favor one over the other.
5	Strongly more important	Experience and judgment strongly favor one over the other.
7	Very strongly more important	Experience and judgment very strongly favor one over the other. Its importance is demonstrated in practice.
9	Extremely more important	The evidence favoring one over the other is of the highest possible validity.
2, 4, 6, 8	Intermediate values	When compromise was needed

Appendix B

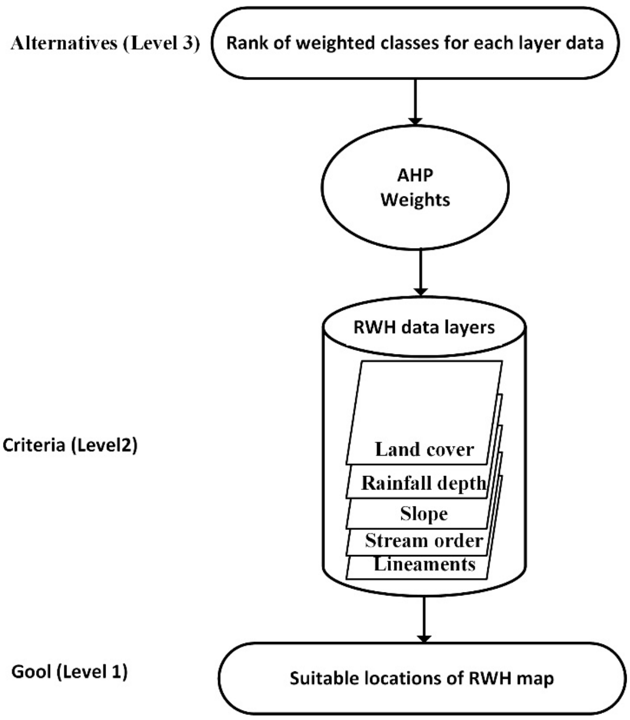

Figure A1. Flow chart of the AHP method for suitable locations for RWH mapping.

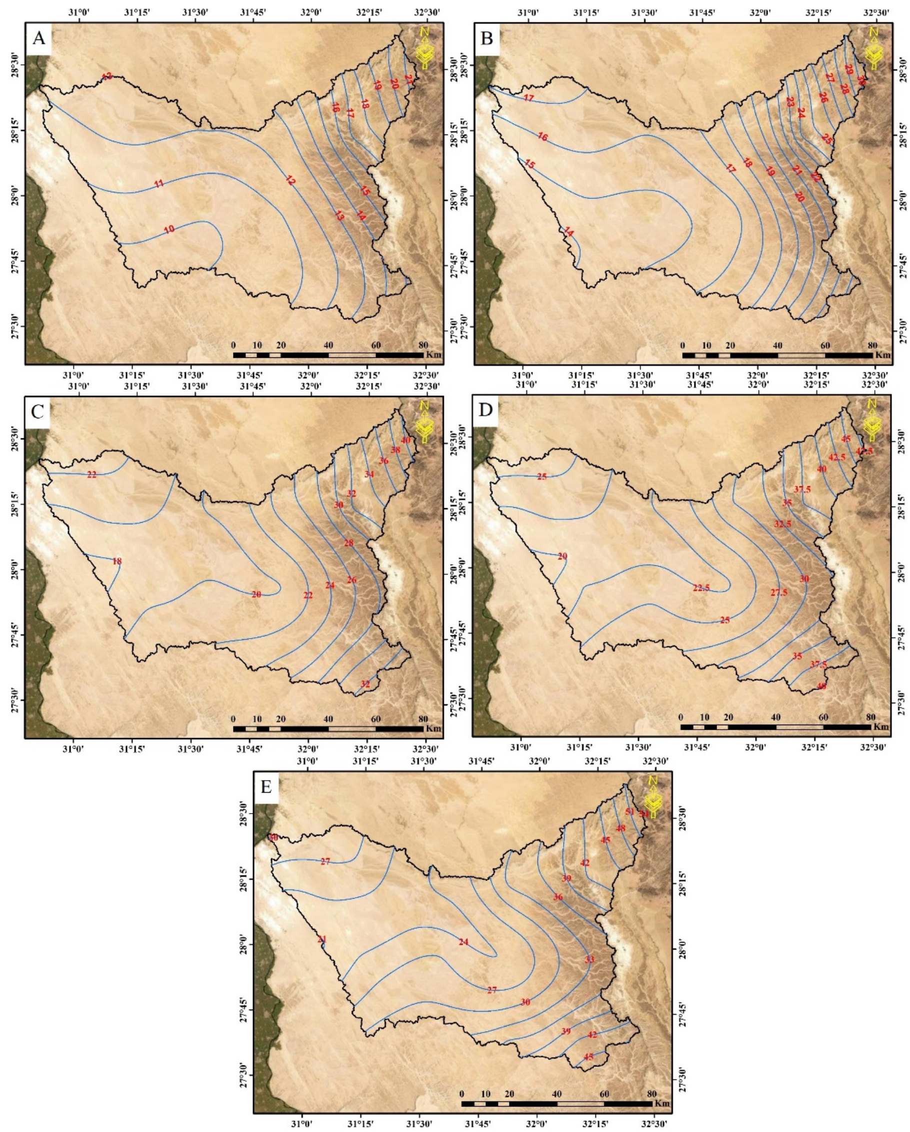

Figure A2. Spatial distribution of maximum 24 h rainfall mm; (**A**) 5-year return period; (**B**) 10-year return period; (**C**) 25-year return period; (**D**) 50-year return periods; (**E**) 100-year return period.

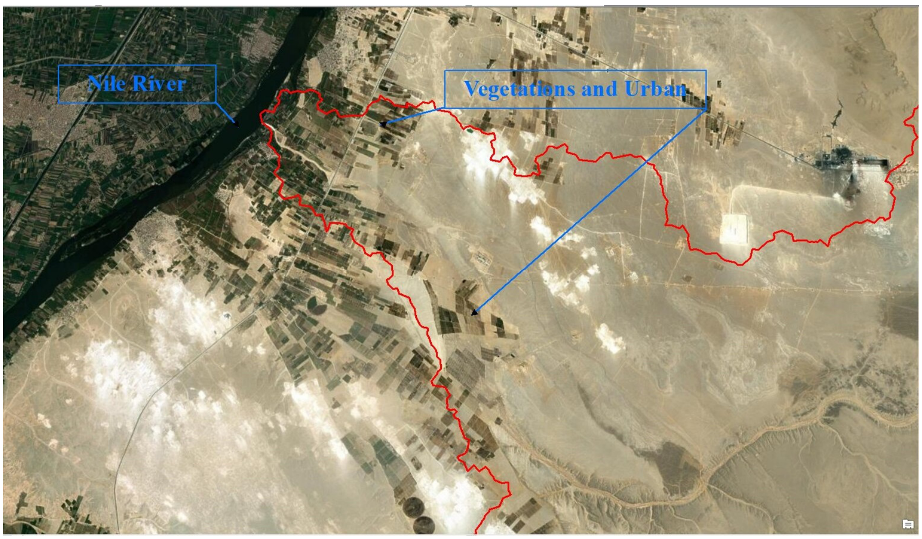

Figure A3. Vegetation and urban area in the study area.

Appendix C

Table A8. Result of linear characteristics of the main basin and its sub-basins.

Basin No	U	1	2	3	4	5	6	7	8	9
1	Nu Lu (km)	2625 556.29	652 275.67	140 149.07	29 82.28	8 56.47	3 13.16	1 7.12		
2	Nu Lu (km)	3505 776.29	877 382.13	172 194.00	41 110.30	11 51.87	2 27.41	1 8.80		
3	Nu Lu (km)	5993 1348.86	1997 669.64	362 318.08	80 168.54	16 81.74	6 37.71	1 33.26		
4	Nu Lu (km)	1843 434.04	519 222.36	123 85.16	24 42.72	5 28.17	2 11.98	1 12.39		
5	Nu Lu (km)	6376 1430.07	2034 669.93	543 348.81	73 182.92	15 89.67	4 30.04	1 39.11		
6	Nu Lu (km)	2447 577.43	604 257.21	138 144.54	36 65.79	8 18.14	2 22.07	1 12.21		
7	Nu Lu (km)	3344 699.06	733 326.43	143 163.55	22 62.02	7 56.98	2 42.07	1 10.49		
8	Nu Lu (km)	2676 549.64	676 244.73	178 155.16	26 54.20	5 53.85	2 5.80	1 11.42		
9	Nu Lu (km)	9213 1994.32	2300 894.01	354 437.24	93 211.35	15 125.83	5 65.09	1 75.56		
10	Nu Lu (km)	9446 2023.56	2123 901.20	386 401.82	90 242.77	22 140.58	4 48.76	1 59.62		
11	Nu Lu (km)	3934 833.14	813 359.14	168 178.75	38 102.65	9 51.98	2 23.56	1 19.43		
12	Nu Lu (km)	4663 972.49	871 440.32	191 206.93	38 114.37	9 66.52	2 34.78	1 7.63		
13	Nu Lu (km)	5612 1176.75	921 540.18	236 269.20	55 137.82	12 87.75	3 16.95	1 29.10		
14	Nu Lu (km)	4553 996.85	881 490.41	204 250.82	54 121.25	12 68.16	3 33.02	1 11.84		
15	Nu Lu (km)	6427 1379.75	1121 650.98	299 302.15	72 170.50	16 104.58	4 22.70	1 39.71		
Main basin	Nu Lu (km)	125,068 27,120.47	29,081 12,688.2	6835 6344	1225 3193	279 1672.78	70 772.08	15 382.19	3 393	1 11.08

Stream order (U), stream number (Nu), stream length km (Lu).

Table A9. Result of the linear characteristics of the main basin and its sub-basins.

Basin No	U	MRb	WMRb	Lb	Lg
1	7	3.80	4.17	23.80	2.55
2	7	4.09	4.21	34.57	2.56
3	7	4.35	3.67	41.87	2.60
4	7	3.70	3.77	28.99	2.63
5	7	8.98	3.55	52.91	2.57
6	7	3.79	4.11	27.02	2.66
7	7	4.14	4.71	53.65	2.43
8	7	4.05	4.08	33.39	2.41
9	7	4.75	4.49	73.56	2.43
10	7	4.64	4.63	63.09	2.42
11	7	4.14	4.82	41.63	2.45
12	7	4.28	5.21	37.16	2.37
13	7	4.31	5.72	44.26	2.30
14	7	4.13	4.98	32.49	2.50
15	7	4.36	5.38	39.63	2.41
Main basin	9	4.40	4.35	177.72	2.47

Stream order (U), mean bifurcation ratio (MRb), weighted mean bifurcation ratio (WMRb), basin length km (Lb), length of overland flow km (Lg).

Table A10. Results of areal characteristics and relief characteristics of the main basin and its sub-basins.

Basin No	A	P	Dd	Fs	T	Rh	BS	Dp
1	223.79	93.66	5.09	15.45	36.92	0.0105	0.0615	Dendritic
2	302.86	113.17	5.12	15.22	40.72	0.0060	0.0411	Dendritic
3	511.88	151.73	5.19	16.52	54.17	0.0063	0.0473	Dendritic
4	159.01	103.37	5.26	15.83	24.35	0.0046	0.0413	Dendritic
5	543.16	196.98	5.14	16.65	45.92	0.0059	0.0406	Dendritic
6	206.29	90.08	5.32	15.69	35.93	0.0048	0.0419	Dendritic
7	280.38	157.98	4.85	15.17	26.91	0.0098	0.0684	Dendritic
8	222.95	103.91	4.82	15.99	34.30	0.0090	0.0703	Dendritic
9	783.91	258.93	4.85	15.28	46.27	0.0083	0.0664	Dendritic
10	789.01	221.50	4.84	15.30	54.50	0.0084	0.0629	Dendritic
11	320.00	132.89	4.90	15.52	37.36	0.0066	0.0457	Dendritic
12	389.19	120.16	4.74	14.84	48.06	0.0074	0.0599	Dendritic
13	490.33	150.54	4.60	13.95	45.44	0.0088	0.1028	Dendritic
14	393.99	117.86	5.01	14.49	48.43	0.0126	0.0652	Dendritic
15	553.10	147.26	4.83	14.36	53.92	0.0171	0.1145	Dendritic
Main basin	10646.40	807.59	4.94	15.27	201.31	0.0070	0.0556	Dendritic

Basin area km^2 (A), basin perimeter km (P), drainage density km/km^2 (Dd), stream frequency km^{-2} (Fs), texture ratio (T), relief ratio (Rh), basin slope degree (BS), drainage patterns (Dp).

Table A11. Calculation of the input parameters of the HEC-HMS model for the basin.

Basin No	A (km^2)	$\Sigma A \times CN$	CNw	S (in)	Ia (in)	BS%	FL (ft)	TL (h)	TC (h)
1	223	15,933.44	71.22	4.04	0.81	6.15	72,377.15	5.08	8.47
2	302	25,157.41	83.07	2.04	0.41	4.11	119,060.67	6.50	10.83
3	511	42,278.18	82.59	2.11	0.42	4.73	178,378.32	8.50	14.17
4	159	11,413.72	71.77	3.93	0.79	4.13	121,821.39	9.27	15.45
5	543	44,544.76	82.01	2.19	0.44	4.06	204,723.68	10.44	17.41
6	206	15,924.80	77.19	2.96	0.59	4.19	94,069.65	6.41	10.68
7	280	23,276.96	83.01	2.05	0.41	6.84	260,557.45	9.44	15.74
8	222	17,573.92	78.83	2.69	0.54	7.03	150,120.48	6.85	11.41
9	783	64,419.36	82.18	2.17	0.43	6.64	356,437.61	12.66	21.10
10	789	62,472.33	79.18	2.63	0.53	6.29	271,505.66	11.50	19.17
11	319	20,926.63	65.40	5.29	1.06	4.57	160,659.67	13.03	21.72
12	389	30,302.01	77.87	2.84	0.57	5.99	160,031.35	8.04	13.40
13	490	40,018.41	81.63	2.25	0.45	10.28	206,709.81	6.70	11.16
14	393	31,334.85	79.54	2.57	0.51	6.52	71,064.32	3.82	6.37
15	553	43,916.03	79.40	2.59	0.52	11.45	164,929.31	5.68	9.47
Mainbasin	10,646	829,384.58	77.90	2.84	0.57	5.56	765,364.20	29.14	48.57

Area (A), curve number (CN), soil moisture (s), initial abstraction (Ia), basin slope (BS), flow length (FL), lag time (TL), time concentration (TC).

Table A12. Weighted RWH-suitable locations ranking in basin.

Decision Factors at Level 2 (i)	Relative Weight at Level 2 of Decision Factor i = RIW2 i	Decision Sub-Factors (j) at Level 3 (Cell Attribute)	Ranking Decision
Land-cover units	0.2085	Vegetation Recent Alluvial Old Alluvial Quarries Limestone with clay Massive limestone	1 2 3 4 5 6
Average of max 24 h rainfall depth (mm)	0.1852	5.875200748–6.75068903 6.750689031–7.658358574 7.658358575–9.030816078 9.030816079–10.76387215 10.76387216–12.63123417	1 2 3 4 5
Slope (degrees)	0.477	0–2.764199904 2.764199905–5.74103057 5.741030571–10.41890733 10.41890734–18.28624552 18.28624553–54.00821351	5 4 3 2 1
Stream order	0.0592	1 2 3 4 5 6 7 8 9	1 2 3 4 5 6 7 8 9
Lineaments density (km/km^2)	0.0701	0–0.206917985 0.206917985–0.389492678 0.389492678–0.614668133 0.614668133–0.912873465 0.912873465–1.55188489	5 4 3 2 1

Table A13. Calculation of the input parameters of the HEC-HMS model for dams.

Basin No	A (km^2)	ΣA × CN	CNw	S (in)	Ia (in)	BS%	FL (ft)	TL (h)	TC (h)
1	52.98	3670.83	69.29	4.43	0.89	3.80	63,692.77	6.15	10.26
2	4747.77	37,9441.81	79.92	2.51	0.50	5.91	729,000.85	25.56	42.60
3	7.53	642.97	85.44	1.70	0.34	10.72	18,217.73	0.83	1.38
4	39.07	3002.85	76.85	3.01	0.60	9.40	52,865.40	2.73	4.54
5	0.85	75.43	88.41	1.31	0.26	7.40	3026.79	0.21	0.35
6	22.17	1935.19	87.29	1.46	0.29	7.11	30,812.99	1.44	2.41
7	4.27	367.02	85.98	1.63	0.33	10.67	15,192.13	0.70	1.17
8	2.12	182.83	86.37	1.58	0.32	8.45	6726.45	0.41	0.68
9	3.99	335.43	84.15	1.88	0.38	15.91	12,422.02	0.52	0.87
10	23.01	1936.89	84.16	1.88	0.38	6.21	37,567.51	2.02	3.37

Area (A), curve number (CN), soil moisture (s), initial abstraction (Ia), basin slope (BS), flow length (FL), lag time (TL), time concentration (TC).

Table A14. Characteristics of proposed dams.

Dam No	Max Elevation (m)	Max Height (m)	Max Storage capacity (m^3)	Max surface area (m^2)
1	107	24	2,653,602.08	291,793.19
2	103	23	10,720,852.86	1,489,698.49
3	565	20	1,629,981.86	296,494.06
4	693	18	1,189,841.62	154,441.31
5	705	17	1,107,544.42	157,873.34
6	660	18	3,421,759.67	501,554.30
7	711	19	2,716,737.12	295,154.51
8	740	22	4,905,677.69	581,781.67
9	710	22	2,277,794.88	261,692.23
10	650	20	2,411,787.02	284,858.42

References

1. Costa, J.E. Hydraulics and Basin Morphometry of the Largest Flash Floods in the Conterminous United States. *J Hydrol.* **1987**, *93*, 313–338. [CrossRef]
2. He, B.; Huang, X.; Ma, M.; Chang, Q.; Tu, Y.; Li, Q.; Zhang, K.; Hong, Y. Analysis of Flash Flood Disaster Characteristics in China from 2011 to 2015. *Nat. Hazards* **2018**, *90*, 407–420. [CrossRef]
3. Abdalla, F.; Shamy, I.E.; Bamousa, A.O.; Mansour, A.; Mohamed, A.; Tahoon, M. Flash Floods and Groundwater Recharge Potentials in Arid Land Alluvial Basins, Southern Red Sea Coast, Egypt. *Int. J. Geosci.* **2014**, *5*, 971–982. [CrossRef]
4. Davies, R. World Disasters Report—Most Deaths Caused by Floods. 2014. Available online: https://floodlist.com/dealing-with-floods/world-disasters-report-100-million-affected-2013 (accessed on 15 October 2022).
5. Dano, U.L. Flash Flood Impact Assessment in Jeddah City: An Analytic Hierarchy Process Approach. *Hydrology* **2020**, *7*, 10. [CrossRef]
6. Prama, M.; Omran, A.; Schröder, D.; Abouelmagd, A. Vulnerability Assessment of Flash Floods in Wadi Dahab Basin, Egypt. *Env. Earth Sci.* **2020**, *79*, 1–17. [CrossRef]
7. Lin, X. Flash Floods in Arid and Semi-Arid Zones. *Tech. Doc. Hydrol.* **1999**. Available online: https://unesdoc.unesco.org/ark:/48223/pf0000118882 (accessed on 15 October 2022).
8. Youssef, A.M.; Pradhan, B.; Hassan, A.M. Flash Flood Risk Estimation along the St. Katherine Road, Southern Sinai, Egypt Using GIS Based Morphometry and Satellite Imagery. *Environ. Earth Sci.* **2011**, *62*, 611–623. [CrossRef]
9. Moawad, M.B.; Aziz, A.O.A.; Mamtimin, B. Flash Floods in the Sahara: A Case Study for the 28 January 2013 Flood in Qena, Egypt. *Geomat. Nat. Hazards Risk* **2016**, *7*, 215–236. [CrossRef]

10. Abdelkader, M.M.; Al-Amoud, A.I.; El-Alfy, M.; El-Feky, A.; Saber, M. Assessment of Flash Flood Hazard Based on Morphometric Aspects and Rainfall-Runoff Modeling in Wadi Nisah, Central Saudi Arabia. *Remote Sens. Appl.* **2021**, *23*, 100562. [CrossRef]
11. Elsebaie, I.H.; el Alfy, M.; Kawara, A.Q. Spatiotemporal Variability of Intensity–Duration–Frequency (IDF) Curves in Arid Areas: Wadi AL-Lith, Saudi Arabia as a Case Study. *Hydrology* **2021**, *9*, 6. [CrossRef]
12. Tizro, A.T.; Voudouris, K.S.; Akbari, K. Simulation of a Groundwater Artificial Recharge in a Semi-Arid Region of Iran. *Irrig. Drain.* **2011**, *60*, 393–403. [CrossRef]
13. Sarma, D.; Xu, Y. The Recharge Process in Alluvial Strip Aquifers in Arid Namibia and Implication for Artificial Recharge. *Hydrogeology* **2017**, *25*, 123–134. [CrossRef]
14. Alataway, A.; El-Alfy, M. Rainwater Harvesting and Artificial Groundwater Recharge in Arid Areas: Case Study in Wadi Al-Alb, Saudi Arabia. *J. Water Resour. Plan. Manag.* **2019**, *145*, 05018017. [CrossRef]
15. Sturm, M.; Zimmermann, M.; Schütz, K.; Urban, W.; Hartung, H. Rainwater Harvesting as an Alternative Water Resource in Rural Sites in Central Northern Namibia. *Phys. Chem. Earth Parts A/B/C* **2009**, *34*, 776–785. [CrossRef]
16. El-Alfy, M. Applications of Engineering Geology on the Geomorphological and Hydrogeological Situations of the Area between Rafah and Ras El-Naqab. Master's Thesis, Mansoura University, Mansoura, Egypt, 1998.
17. Escalante, E.F.; Gil, R.C.; Fraile, M.Á.S.M.; Serrano, F.S. Economic Assessment of Opportunities for Managed Aquifer Recharge Techniques in Spain Using an Advanced Geographic Information System (GIS). *Water* **2014**, *6*, 2021–2040. [CrossRef]
18. Qi, Q.; Marwa, J.; Mwamila, T.B.; Gwenzi, W.; Noubactep, C. Making Rainwater Harvesting a Key Solution for Water Management: The Universality of the Kilimanjaro Concept. *Sustainability* **2019**, *11*, 5606. [CrossRef]
19. Ammar, A.; Riksen, M.; Ouessar, M.; Ritsema, C. Identification of Suitable Sites for Rainwater Harvesting Structures in Arid and Semi-Arid Regions: A Review. *Int. Soil Water Conserv. Res.* **2016**, *4*, 108–120. [CrossRef]
20. Musaed, H.A.H.; Al-Bassam, A.M.; Zaidi, F.K.; Alfaifi, H.J.; Ibrahim, E. Hydrochemical Assessment of Groundwater in Mesozoic Sedimentary Aquifers in an Arid Region: A Case Study from Wadi Nisah in Central Saudi Arabia. *Environ. Earth Sci.* **2020**, *79*, 1–12. [CrossRef]
21. El-Alfy, M.; Merkel, B. Hydrochemical Relationships and Geochemical Modeling of Ground Water in Al Arish Area, North Sinai, Egypt. *Hydrol. Sci. Technol.* **2006**, *22*, 47–62.
22. El-Alfy, M. Hydrochemical Modeling and Assessment of Groundwater Contamination in Northwest Sinai, Egypt. *Water Environ. Res.* **2013**, *85*, 211–223. [CrossRef]
23. Mahmoud, S.H.; Alazba, A.A.; Adamowski, J.; El-Gindy, A.M. GIS Methods for Sustainable Stormwater Harvesting and Storage Using Remote Sensing for Land Cover Data—Location Assessment. *Environ. Monit. Assess.* **2015**, *187*, 1–19. [CrossRef]
24. Balkhair, K.S.; Ur Rahman, K. Development and Assessment of Rainwater Harvesting Suitability Map Using Analytical Hierarchy Process, GIS and RS Techniques. *Geocarto. Int.* **2021**, *36*, 421–448. [CrossRef]
25. Ouali, L.; Hssaisoune, M.; Kabiri, L.; Slimani, M.M.; el Mouquaddam, K.; Namous, M.; Arioua, A.; ben Moussa, A.; Benqlilou, H.; Bouchaou, L. Mapping of Potential Sites for Rainwater Harvesting Structures Using GIS and MCDM Approaches: Case Study of the Toudgha Watershed, Morocco. *EuroMediterr. J. Env. Integr.* **2022**, *7*, 49–64. [CrossRef]
26. El-Magd, S.A.A.; Pradhan, B.; Alamri, A. Machine Learning Algorithm for Flash Flood Prediction Mapping in Wadi El-Laqeita and Surroundings, Central Eastern Desert, Egypt. *Arab. J. Geosci.* **2021**, *14*, 1–14. [CrossRef]
27. Taha, M.M.N.; Elbarbary, S.M.; Naguib, D.M.; El-Shamy, I.Z. Flash Flood Hazard Zonation Based on Basin Morphometry Using Remote Sensing and GIS Techniques: A Case Study of Wadi Qena Basin, Eastern Desert, Egypt. *Remote Sens. Appl.* **2017**, *8*, 157–167. [CrossRef]
28. El-Bastawesy, M.; Abu El Ella, E.M. Quantitative Estimates of Flash Flood Discharge into Waste Water Disposal Sites in Wadi Al Saaf, the Eastern Desert of Egypt. *J. Afr. Earth Sci.* **2017**, *136*, 312–318. [CrossRef]
29. Abbas, M.; Carling, P.A.; Jansen, J.D.; Al-Saqarat, B.S. Flash-Flood Hydrology and Aquifer-Recharge in Wadi Umm Sidr, Eastern Desert, Egypt. *J. Arid Environ.* **2020**, *178*, 104170. [CrossRef]
30. Harmsen, J. A New and Scalable Approach for Rural Sanitation in Egypt: The Deir Gabal El-Tair Pilot. The Environmental Technology for Impact Conference (ETEI2015). 2016. Available online: https://scholar.google.com/scholar?hl=en&as_sdt=0%2C5&q=A+New+and+Scalable+Approach+for+Rural+Sanitation+in+Egypt%3A+The+Deir+Gabal+El-Tair+Pilot&btnG= (accessed on 15 October 2022).
31. Khalil, M.; Abotalib, A.; Farag, M.; Rabei, M.; Abdelhady, A.A.; Pichler, T. Poor Drainage-Induced Waterlogging in Saharan Groundwater-Irrigated Lands: Integration of Geospatial, Geophysical, and Hydrogeological Techniques. *Catena* **2021**, *207*, 105615. [CrossRef]
32. Moneim, A.A.A. Overview of the Geomorphological and Hydrogeological Characteristics of the Eastern Desert of Egypt. *Hydrogeol. J.* **2005**, *13*, 416–425. [CrossRef]
33. El-Saadawy, O.; Gaber, A.; Othman, A.; Abotalib, A.Z.; Bastawesy, M.E.; Attwa, M. Modeling Flash Floods and Induced Recharge into Alluvial Aquifers Using Multi-Temporal Remote Sensing and Electrical Resistivity Imaging. *Sustainability* **2020**, *12*, 10204. [CrossRef]
34. Mapping Products | GIS Software Products—Esri. Available online: https://www.esri.com/en-us/arcgis/products/index (accessed on 15 October 2022).
35. ERDAS IMAGINE 2015 (64-Bit). Available online: https://download.hexagongeospatial.com/en/downloads/imagine/erdas-imagine-2015-64-bit (accessed on 15 October 2022).

36. HYFRAN 1.2 Download (Free Trial)—Hyfran.Exe. Available online: https://hyfran.software.informer.com/1.2/ (accessed on 15 October 2022).
37. WMS Downloads | Aquaveo.Com. Available online: https://www.aquaveo.com/downloads-wms?s=WMS&v=11.0 (accessed on 15 October 2022).
38. HEC-HMS Downloads. Available online: https://www.hec.usace.army.mil/software/hec-hms/downloads.aspx (accessed on 15 October 2022).
39. About Us—CATALYST.Earth. Available online: https://catalyst.earth/about/ (accessed on 15 October 2022).
40. ITT Visual Information Solutions | Make Informed Decisions. Available online: https://www.ittvis.com/ (accessed on 15 October 2022).
41. RockWorks16—RockWare. Available online: https://www.rockware.com/demo_downloads/rockworks16/ (accessed on 15 October 2022).
42. el Kenawy, A.M.; Lopez-Moreno, J.I.; McCabe, M.F.; Robaa, S.M.; Domínguez-Castro, F.; Peña-Gallardo, M.; Trigo, R.M.; Hereher, M.E.; Al-Awadhi, T.; Vicente-Serrano, S.M. Daily Temperature Extremes over Egypt: Spatial Patterns, Temporal Trends, and Driving Forces. *Atmos. Res.* **2019**, *226*, 219–239. [CrossRef]
43. Mestre, O.; Domonkos, P.; Picard, F.; Auer, I.; Robin, S. HOMER: A Homogenization Software–Methods and Applications. 2013. Available online: https://scholar.google.com/scholar?hl=en&as_sdt=0%2C5&q=HOMER%3A+A+Homogenization+Software%E2%80%93Methods+and+Applications&btnG= (accessed on 15 October 2022).
44. Saha, S.; Moorthi, S.; Pan, H.; Wu, X.; Wang, J.; Nadiga, S.; Goldberg, M. The NCEP Climate Forecast System Reanalysis. *Bull. Am. Meteorol. Soc.* **2010**, *91*, 1015–1058. [CrossRef]
45. El-Kenawy, A.M.; al Buloshi, A.; al Awadhi, T.; al Nasiri, N.; Navarro-Serrano, F.; Alhatrushi, S.; Robaa, S.M.; Domínguez-Castro, F.; McCabe, M.F.; Schuwerack, P.M.; et al. Evidence for Intensification of Meteorological Droughts in Oman over the Past Four Decades. *Atmos. Res.* **2020**, *246*, 105126. [CrossRef]
46. El-Kenawy, A.; López-Moreno, J.I.; Stepanek, P.; Vicente-Serrano, S.M. An Assessment of the Role of Homogenization Protocol in the Performance of Daily Temperature Series and Trends: Application to Northeastern Spain. *Int. J. Climatol.* **2013**, *33*, 87–108. [CrossRef]
47. Horton, R.E. Erosional Development of Streams and Their Drainage Basins; Hydrophysical Approach to Quantitative Morphology. *Geol. Soc. Am. Bull.* **1945**, *56*, 275–370. [CrossRef]
48. Strahler, A.N. Revisions of Horton's Quantitative Factors in Erosional Terrain. *Trans. Am. Geophys. Union* **1953**, *34*, 345.
49. Schumm, S.A. Evolution of Drainage Systems and Slopes in Badlands at Perth Amboy, New Jersey. *Geol. Soc. Am. Bull.* **1956**, *67*, 597–646. [CrossRef]
50. Strahler, A.N. Quantitative Geomorphology of Drainage Basin and Channel Networks. *Handb. Appl. Hydrol.* **1964**. Available online: https://scholar.google.com/scholar?hl=en&as_sdt=0%2C5&q=Quantitative+Geomorphology+of+Drainage+Basin+and+Channel+Networks&btnG= (accessed on 15 October 2022).
51. Horton, R.E. Drainage-Basin Characteristics. *Trans. Am. Geophys. Union* **1932**, *13*, 350–361. [CrossRef]
52. Taylor, A.B.; Schwarz, H.E. Unit-hydrograph Lag and Peak Flow Related to Basin Characteristics. *Eos Trans. Am. Geophys. Union* **1952**, *33*, 235–246. [CrossRef]
53. Melton, M.A. An Analysis of the Relations among Elements of Climate, Surface Properties, and Geomorphology. *Columbia Univ. N. Y.* **1957**. Available online: https://apps.dtic.mil/sti/pdfs/AD0148373.pdf (accessed on 15 October 2022).
54. Farhan, Y.; Anbar, A.; Enaba, O.; Al-Shaikh, N. Quantitative Analysis of Geomorphometric Parameters of Wadi Kerak, Jordan, Using Remote Sensing and GIS. *J. Water Resour. Prot.* **2015**, *07*, 456–475. [CrossRef]
55. Mahmood, S.; Rahman, A. Flash Flood Susceptibility Modeling Using Geo-Morphometric and Hydrological Approaches in Panjkora Basin, Eastern Hindu Kush, Pakistan. *Environ. Earth Sci.* **2019**, *78*, 1–16. [CrossRef]
56. Davis, J.; Sampson, R. Statistics and Data Analysis in Geology. 1986. Available online: https://www.kgs.ku.edu/Mathgeo/Books/Stat/ClarifyEq4-81.pdf (accessed on 15 October 2022).
57. Hasmadi, M.; Pakhriazad, H.Z.; Shahrin, M.F. Evaluating Supervised and Unsupervised Techniques for Land Mapping Using Remote Sensing Data. *Geogr. Malays. J. Soc. Space* **2009**, *5*, 1–10.
58. Abburu, S.; Golla, S.B. Satellite Image Classification Methods and Techniques: A Review. *Int. J. Comput. Appl.* **2015**, *119*, 1–6. [CrossRef]
59. Cronshey, R.; Roberts, R.; Miller, N. Urban Hydrology for Small Watersheds (TR-55 Rev.). *Hydraul. Hydrol. Small Comput. Age* **1985**, 1268–1273. Available online: https://cedb.asce.org/CEDBsearch/record.jsp?dockey=0045976 (accessed on 15 October 2022).
60. Gheith, H.; Sultan, M. Construction of a Hydrologic Model for Estimating Wadi Runoff and Groundwater Recharge in the Eastern Desert, Egypt. *J. Hydrol.* **2002**, *263*, 36–55. [CrossRef]
61. Kamali, B.; Mousavi, S.J.; Abbaspour, K.C. Automatic Calibration of HEC-HMS Using Single-Objective and Multi-Objective PSO Algorithms. *Hydrol. Process.* **2013**, *27*, 4028–4042. [CrossRef]
62. Fleming, M. Description of the Hydrologic Engineering Center's Hydrologic Modeling System (HEC-HMS) and Application to Watershed Studies. *Eng. Res. Dev. Cent. Vicksbg. Ms.* **2004**. Available online: https://scholar.google.com/scholar?hl=en&as_sdt=0%2C5&q=Description+of+the+Hydrologic+Engineering+Center%E2%80%99s+Hydrologic+Modeling+System+%28HEC-HMS%29+and+Application+to+Watershed+Studies&btnG= (accessed on 15 October 2022).

63. De-Simas, M.J.C. Lag-Time Characteristics in Small Watersheds in the United States. *Univ. Ariz.* **1996**. Available online: https://scholar.google.com/scholar?hl=en&as_sdt=0%2C5&q=Lag-Time+Characteristics+in+Small+Watersheds+in+the+United+States&btnG= (accessed on 15 October 2022).
64. Cronshey, R. Urban Hydrology for Small Watersheds. *US Dept. Agric. Soil Conserv. Serv. Eng. Div.* **1986**. Available online: https://tamug-ir.tdl.org/handle/1969.3/24438 (accessed on 15 October 2022).
65. Orencio, P.M.; Fujii, M. A Localized Disaster-Resilience Index to Assess Coastal Communities Based on an Analytic Hierarchy Process (AHP). *Int. J. Disaster Risk Reduct.* **2013**, *3*, 62–75. [CrossRef]
66. Ekmekcioğlu, Ö.; Koc, K.; Özger, M. Stakeholder Perceptions in Flood Risk Assessment: A Hybrid Fuzzy AHP-TOPSIS Approach for Istanbul, Turkey. *Int. J. Disaster Risk Reduct.* **2021**, *60*, 102327. [CrossRef]
67. Ekmekcioğlu, Ö.; Koc, K.; Özger, M. Towards Flood Risk Mapping Based on Multi-Tiered Decision Making in a Densely Urbanized Metropolitan City of Istanbul. *Sustain. Cities Soc.* **2022**, *80*, 103759. [CrossRef]
68. Estoque, R.C.; Murayama, Y. Suitability Analysis for Beekeeping Sites in La Union, Philippines, Using GIS and Multi-Criteria Evaluation Techniques. *Res. J. Appl. Sci.* **2010**, *5*, 242–253. [CrossRef]
69. Ouma, Y.O.; Tateishi, R. Urban Flood Vulnerability and Risk Mapping Using Integrated Multi-Parametric AHP and GIS: Methodological Overview and Case Study Assessment. *Water* **2014**, *6*, 1515–1545. [CrossRef]
70. Xiao, Y.; Yi, S.; Tang, Z. Integrated Flood Hazard Assessment Based on Spatial Ordered Weighted Averaging Method Considering Spatial Heterogeneity of Risk Preference. *Sci. Total Environ.* **2017**, *599*, 1034–1046. [CrossRef]
71. Saaty, R.W. The Analytic Hierarchy Process—What It Is and How It Is Used. *Math. Model.* **1987**, *9*, 161–176. [CrossRef]
72. Zavadskas, E.K.; Vilutienė, T.; Turskis, Z.; Šaparauskas, J. Multi-Criteria Analysis of Projects' Performance in Construction. *Arch. Civ. Mech. Eng.* **2014**, *14*, 114–121. [CrossRef]
73. Kazakis, N.; Kougias, I.; Patsialis, T. Assessment of Flood Hazard Areas at a Regional Scale Using an Index-Based Approach and Analytical Hierarchy Process: Application in Rhodope-Evros Region, Greece. *Sci. Total Environ.* **2015**, *538*, 555–563. [CrossRef]
74. Papaioannou, G.; Vasiliades, L.; Loukas, A. Multi-Criteria Analysis Framework for Potential Flood Prone Areas Mapping. *Water Resour. Manag.* **2015**, *29*, 399–418. [CrossRef]
75. Hajeeh, M. Application of the Analytical Hierarchy Process in the Selection of Desalination Plants. *Desalination* **2005**, *174*, 97–108. [CrossRef]
76. Gajbhiye, S.; Mishra, S.K.; Pandey, A. Prioritizing Erosion-Prone Area through Morphometric Analysis: An RS and GIS Perspective. *Appl. Water Sci.* **2014**, *4*, 51–61. [CrossRef]
77. Pareta, K.; Pareta, U. Quantitative Morphometric Analysis of a Watershed of Yamuna Basin, India Using ASTER (DEM) Data and GIS. *Int. J. Geomat. Geosci.* **2011**, *2*, 248.